

# Amplifying the differences in aluminium-based eutectic electrolytes through electrodeposition on MXenes

*Wei Ying Lieu<sup>1,2†</sup>, Anupma Thakur<sup>3,4†</sup>, Sonal Kumar<sup>1†</sup>, Yuanjian Li<sup>1</sup>, Xue Liang Li<sup>2</sup>, Yixiang Li<sup>2</sup>, Gaoliang Yang<sup>1</sup>, Yifan Li<sup>2</sup>, Tanmay Ghosh<sup>1</sup>, Man-Fai Ng<sup>5</sup>, Babak Anasori<sup>3,4,6\*</sup>, Hui Ying Yang<sup>2\*</sup>, Zhi Wei Seh<sup>1\*</sup>*

<sup>1</sup>Institute of Materials Research and Engineering (IMRE), Agency for Science, Technology and Research (A\*STAR), 2 Fusionopolis Way, Innovis #08-03, Singapore 138634, Republic of Singapore

\*Email: sehzw@imre.a-star.edu.sg

<sup>2</sup>Singapore University of Technology and Design, Pillar of Engineering Product Development, 8 Somapah Road, Singapore 487372, Republic of Singapore

\*E-mail: yanghuiying@sutd.edu.sg

<sup>3</sup>Department of Mechanical and Energy Engineering, and Integrated Nanosystems Development Institute (INDI), Purdue School of Engineering and Technology, Indiana University-Purdue University Indianapolis, Indianapolis 46202, USA

<sup>4</sup>School of Materials Engineering, Purdue University, 701 W Stadium Ave, West Lafayette, IN, 47907, USA

\*E-mail: banasori@purdue.edu

<sup>5</sup>Institute of High Performance Computing (IHPC), Agency for Science, Technology and Research (A\*STAR), 1 Fusionopolis Way, #16-16 Connexis, Singapore 138632, Republic of Singapore

<sup>6</sup>School of Mechanical Engineering, Purdue University, West Lafayette, IN, 47907, USA

† These authors contributed equally to this work.

Keywords: Aluminium batteries, eutectic mixtures, 1-Ethyl-3-methylimidazolium chloride (EMImCl)/AlCl<sub>3</sub> electrolyte, urea/AlCl<sub>3</sub> electrolyte, MXenes.

## Abstract

Traditionally, rechargeable lithium metal battery systems relied on simple metal cationic species to enable metal nucleation and deposition. However, this mechanism is less applicable to room-temperature rechargeable aluminium batteries (RABs), which utilise complex ionic species. In this work, we take advantage of two different MXenes,  $\text{Mo}_2\text{Ti}_2\text{C}_3\text{T}_x$  and  $\text{Ti}_3\text{C}_2\text{T}_x$ , which have different metal-termination group bond strengths, interlayer spacings, and surface termination compositions, to amplify and visualise the differences between two promising RAB electrolytes (i.e., urea/ $\text{AlCl}_3$  and EMImCl/ $\text{AlCl}_3$ ). This work allowed us to deduce the following: (1) despite lower coulombic efficiencies, smoother Al deposits were observed when the urea/ $\text{AlCl}_3$  electrolyte is used; (2) unknown side reactions occur in all the different scenarios, however, they are likely less reversible in the EMImCl/ $\text{AlCl}_3$  electrolyte; (3) metal-halogen exchange reactions can occur in all scenarios, forming  $\text{Al}(\text{OF})_x$  and  $\text{AlF}_x$  species; (4) the free urea in urea/ $\text{AlCl}_3$  electrolyte behaves differently from the urea in aqueous solutions. Overall, due to the characteristics of aluminium, RABs involve vastly different internal mechanisms, resulting in the need for audacious attempts towards system understanding.

## Introduction

Rechargeable batteries have become an important aspect of today's world. However, with limited lithium (Li) resources, it has become critical for us to explore other alternative metals such as sodium (Na), potassium (K), magnesium (Mg), calcium (Ca), zinc (Zn), and aluminium (Al) to be incorporated into rechargeable battery systems.<sup>1,2</sup> Amongst these metals, Al is the most abundant metal on earth that also exhibits a high theoretical volumetric capacity (8046 mAh/cm<sup>3</sup>) and a theoretical specific capacity (2981 mAh/g).<sup>3,4</sup> Despite its potential, modern Al-based battery research is still mostly in the nascent stage, largely because of the dearth of suitable electrolytes that can easily integrate with Al metal and the corresponding electrode components.

Proper battery electrolytes should be developed to be compatible with electrodes, which means that new battery electrode chemistries can bring about new electrolyte compositions.<sup>5</sup> However, electrolyte improvements have largely involved minimal changes to the main skeletal electrolyte compositions, relying on ion-solvation structure modifications, and the design and use of additives to improve compatibility.<sup>6,7</sup> Such incremental changes have served well for numerous monovalent-ion battery chemistries as they are generally reliant on simple metal cationic species for metal nucleation, in which metal ions (e.g., Li<sup>+</sup>, Na<sup>+</sup>, and K<sup>+</sup>) from the electrolyte undergo a simple reduction to effectively deposit on the current collector. Among different battery types, this mechanism is less applicable to multivalent-ion batteries such as rechargeable Al batteries (RABs). While Al<sup>3+</sup> ions have been found in aqueous Al batteries, Al electrodeposition rarely takes place in aqueous solutions due to the lower reduction potential of Al<sup>3+</sup>/Al with respect to H<sub>2</sub>O/H<sub>2</sub>.<sup>8,9</sup> Furthermore, the high charge density of Al<sup>3+</sup> ion is also an indication of the difficulty involved in finding a reliable cathode for aqueous Al batteries as stronger electrostatic attractions involved during Al<sup>3+</sup> ion extraction and intercalation have been reported to result in the structural collapse of cathodes,<sup>10</sup> thus potentially restricting the future possibilities of Al batteries.

To mitigate the potential pitfalls of using aqueous electrolytes, researchers have attempted to use eutectic electrolytes in RABs. These electrolytes are often composed of two or more components that interact with each other when there are sufficient intermolecular forces of attraction, forming a more viscous and less volatile electrolyte system with a larger electrochemical stability window than aqueous aluminium batteries.<sup>11</sup> The 1-ethyl-3-methylimidazolium chloride (EMImCl)/AlCl<sub>3</sub> electrolyte system was first proposed by Archer and colleagues in 2011 and further refined by Dai's group in 2015.<sup>12-15</sup> In contrast to the simple

cationic nucleation mechanism, room-temperature eutectic electrolyte systems rely on the reduction of complex ions ( $\text{Al}_2\text{Cl}_7^-$  ions) in the electrolyte for nucleation and the insertion of complex  $\text{AlCl}_4^-$  ions for cathodic reactions, increasing its complexity.<sup>16,17</sup> Nonetheless, practical problems specific to the EMImCl/ $\text{AlCl}_3$  electrolyte also exist. Existing research has shown that the EMImCl/ $\text{AlCl}_3$  electrolyte is costly and substantially corrosive, which will be inhibitory towards future commercialisation.<sup>18-21</sup> This resulted in researchers proposing other alternative eutectic electrolyte systems, such as the urea/ $\text{AlCl}_3$ , acetamide/ $\text{AlCl}_3$ , and EMImBr/ $\text{AlCl}_3$  electrolytes.<sup>22-25</sup> Amongst them, the urea/ $\text{AlCl}_3$  system was deemed to be a promising alternative system. Unlike the EMImCl/ $\text{AlCl}_3$  system that had an excess of  $\text{Cl}^-$  ions which enabled the formation of  $\text{AlCl}_4^-$  and  $\text{Al}_2\text{Cl}_7^-$  ions, the clear and colourless urea/ $\text{AlCl}_3$  system allows  $\text{Al}_2\text{Cl}_6$  (empirical  $\text{AlCl}_3$ ) to be heterolytically cleaved to form  $\text{AlCl}_4^-$  anions and  $[\text{AlCl}_2\cdot(\text{urea})_2]^+$  cations. Together with the  $\text{Al}_2\text{Cl}_7^-$  ions formed from excess  $\text{AlCl}_3$ , these  $[\text{AlCl}_2\cdot(\text{urea})_2]^+$  ions were previously determined to enable the deposition of metallic Al as  $\text{AlCl}_4^-$  ions continue to take part in cathodic reactions (**Figure 1a**).<sup>26,27</sup>

While the prowess of different eutectic systems has been demonstrated in individual reports, few works have sought to elucidate pragmatic differences amongst the electrolytes apart from their chemical compositions and the occasional electrochemical performances.<sup>28</sup> This lack of studies is regrettable as a good comprehension of fundamental electrolyte chemistries has always been important in fabricating good batteries. Furthermore, unlike conventional battery electrolytes where additives can be added easily, an ill-conceived addition of additives can have a large impact on the electrolyte's eutectic point,<sup>29,30</sup> henceforth affecting the electrolyte's viscosity and conductivity, rendering the trial-and-error process of additive engineering significantly more convoluted and undesirable. Therefore, to avoid resource wastage, it is imperative for us to progressively understand the underlying chemistries, starting from accentuating the pragmatic differences among electrolytes.

A potential electrode material that can help to amplify the difference in the electrolytes is two-dimensional (2D) MXenes. MXenes are a family of 2D transition-metal carbides, nitrides, or carbonitrides that have been observed to have high electrical conductivity (up to 24000 S/cm), unique surface terminations ( $-\text{F}$ ,  $-\text{Cl}$ ,  $=\text{O}$ ,  $-\text{OH}$ ), and high mechanical stiffness ( $326 \pm 29$  N/m).<sup>31-33</sup> Typically synthesised from their MAX phases through selective etching, with M representing a transition metal, A representing the main group element A (e.g., Al, Si, Ga), and X representing C, N, or CN.<sup>34</sup> Depending on the selective etching method used, the obtained MXenes can have a range of surface terminations. In the recent decade, MXenes has become a

popular electrode material used in battery research and has consistently proved its mettle in other existing battery systems, particularly as an anode host that permits uniform and reversible metal plating/stripping.<sup>35-39</sup> However, the mechanism of RABs with MXenes electrodes is usually not well understood and dissimilar reports have been occasionally published. For instance, Guan et al. reported that  $\text{Ti}_3\text{C}_2\text{T}_x$  MXene enables a “dead zone” to be formed when there are significant amounts of  $-\text{OH}$  and  $-\text{COOH}$  surface termination groups, thus allowing MXene to act as a reliable current collector as  $\text{AlCl}_4^-$  ion intercalation is prevented.<sup>40</sup> A similar report was also made by Yuan et al. which assumes that MXene is an inert support material.<sup>41</sup> However, this is in contrast with other reports which suggest that  $\text{AlCl}_4^-$  ions and  $\text{Al}^{3+}$  ions can intercalate between MXene sheets or be in proximity to the MXene surface.<sup>42-44</sup> Hence, this shows that there needs to be a deeper understanding before we can adequately utilise MXenes in RABs, contrasting with the plug-and-play characteristic of MXenes that is usually applied in other battery systems.

For the first time, to amplify and study the differences between two popular RAB eutectic electrolyte systems (i.e.,  $\text{EMImCl}/\text{AlCl}_3$  and  $\text{urea}/\text{AlCl}_3$ ), we sought to conduct Al electrodeposition on the double transition metal MXene,  $\text{Mo}_2\text{Ti}_2\text{C}_3\text{T}_x$ , and the conventional  $\text{Ti}_3\text{C}_2\text{T}_x$  MXene film, as demonstrated in **Figure 1b**. **To the best of our knowledge, this work is the first study to concretely evidence the possible side reactions in both electrolytes, as well as the first demonstration of Al electrodeposition on  $\text{Mo}_2\text{Ti}_2\text{C}_3\text{T}_x$  in RABs, which is less widely explored compared to traditional  $\text{Ti}_3\text{C}_2\text{T}_x$  MXene.** As molybdenum (Mo) is known to have a larger electron cloud than titanium (Ti), it is expected that the bonds between Mo and termination groups are stronger than the Ti-termination group bonds. Furthermore, although both MXene films are synthesised from the chemical etching from their respective MAX phases, experimental data shows that  $\text{Mo}_2\text{Ti}_2\text{C}_3\text{T}_x$  MXene has a larger interlayer spacing and lower fluorine content than  $\text{Ti}_3\text{C}_2\text{T}_x$  MXenes. These are factors that consequentially translate into observations regarding side reaction, species intercalation, and surface adsorption viability in non-aqueous eutectic Al electrolytes, which resulted in their incorporation. Based on our work, we conclude that while metallic Al deposition occurs in all four experimental scenarios, the process and species behaviour involved varies, hence resulting in different final morphologies and electrochemical behaviour. Better Al electrodeposition was observed on the  $\text{Mo}_2\text{Ti}_2\text{C}_3\text{T}_x$  film in  $\text{urea}/\text{AlCl}_3$ , but the same holds on the  $\text{Ti}_3\text{C}_2\text{T}_x$  film in  $\text{EMImCl}/\text{AlCl}_3$ , evidencing distinctive differences between the two electrolytes.

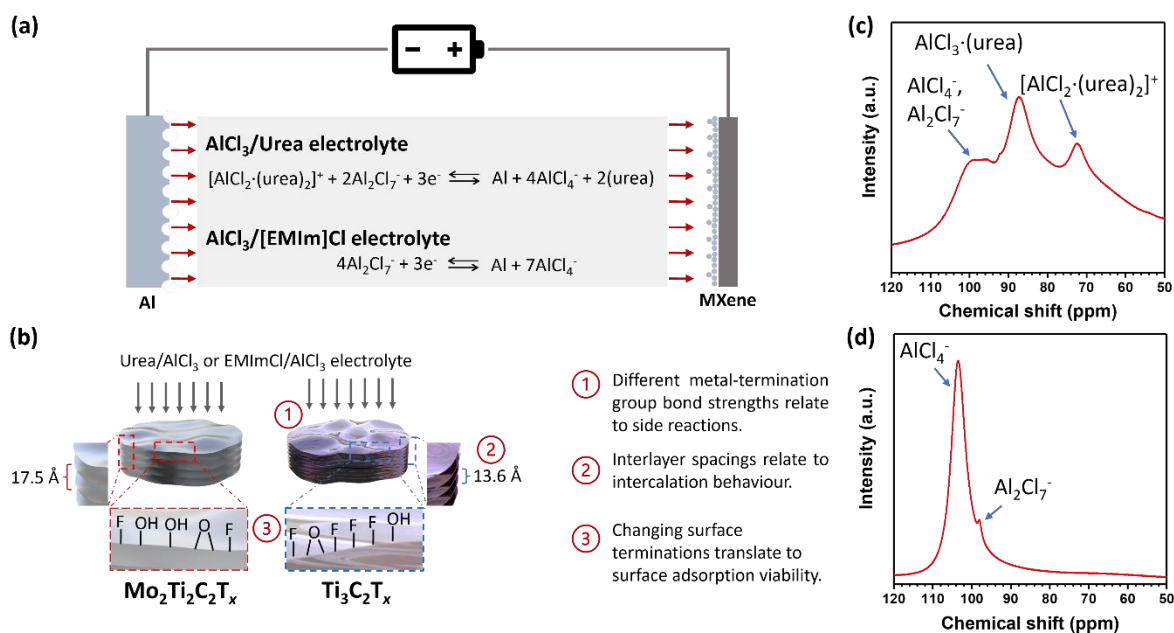


**Figure 1.** (a) Reaction mechanism of the different electrolytes with red arrows denoting the plating process of Al on MXene. (b) Schematic to demonstrate Al deposition on the two different MXenes using two different deep eutectic solvent electrolytes.  $\text{Mo}_2\text{Ti}_2\text{C}_2\text{T}_x$  and  $\text{Ti}_3\text{C}_2\text{T}_x$  MXenes were chosen due to their different elemental composition, interlayer spacing, and surface termination compositions.  $^{27}\text{Al}$  NMR spectrum of the (c) urea/ $\text{AlCl}_3$  and the (d) EMImCl/ $\text{AlCl}_3$  electrolytes used with the associated electrolyte components.

## Results and Discussion

### Aluminium-based Eutectic Electrolytes

Mixing anhydrous EMImCl and anhydrous  $\text{AlCl}_3$  powders together in 1:1.3 ratio gave a clear, yellowish solution, whereas mixing vacuum-dried urea and anhydrous  $\text{AlCl}_3$  powders at a ratio of 1:1.3 gave a clear, colourless solution. In agreement with previous reports, this difference in ionic compositions was observed experimentally through the  $^{27}\text{Al}$  NMR spectra, in which the urea/ $\text{AlCl}_3$  system was observed to consist of the  $\text{AlCl}_4^-$  and  $\text{Al}_2\text{Cl}_7^-$  anions, the neutral  $\text{AlCl}_3 \cdot (\text{urea})$ , and the cationic  $[\text{AlCl}_2 \cdot (\text{urea})_2]^+$  species. This is in contrast with the EMImCl/ $\text{AlCl}_3$  spectrum, where only  $\text{AlCl}_4^-$  and  $\text{Al}_2\text{Cl}_7^-$  anions were observed (**Figure 1c, d**).

<sup>45</sup> Given the innate composition differences between the two electrolytes, assuming these electrolytes function similarly in a battery without thorough studies might eventually arise as a major flaw.

## MXene and its properties

The  $\text{Mo}_2\text{Ti}_2\text{C}_3\text{T}_x$  and  $\text{Ti}_3\text{C}_2\text{T}_x$  MXene suspensions were vacuum-filtrated and freeze-dried to obtain the resulting free-standing films in **Figures 2a and S1**. The (00 $l$ ) peaks of  $\text{Mo}_2\text{Ti}_2\text{C}_3\text{T}_x$  and  $\text{Ti}_3\text{C}_2\text{T}_x$  films were observed in the X-ray diffraction (XRD) patterns after vacuum filtration, further confirming the respective identities of the individual films (**Figure 2b**). Based on the (002) peaks, it was derived that the d-spacings of  $\text{Mo}_2\text{Ti}_2\text{C}_3\text{T}_x$  and  $\text{Ti}_3\text{C}_2\text{T}_x$  MXenes, which are the sums of the MXene single-layer flake thickness and the interlayer spacings, are approximately 17.5 Å and 13.6 Å respectively. **A close study of the MXene interlayer spacings after being exposed to electrolytes is important as it was previously reported that MXenes can enable the degradation of urea into ammonium cations and carbon dioxide gas given the right conditions.**<sup>46</sup> Hence, it should not be presumed that MXenes are compatible with the urea/ $\text{AlCl}_3$  system that potentially contains free urea. If the urea degrades during the aluminium plating or stripping process, the intercalation of ammonium cations will occur, resulting in a shift in the XRD peak, indicating the expansion of interlayer spacing, allowing the viability of MXenes in urea/ $\text{AlCl}_3$  electrolyte to be further assessed. Thereafter, quantitative analyses based on X-ray photoelectron spectroscopy (XPS) were conducted to gain a clearer distinction between the 2 MXene films in terms of their surface terminations and atomic contents (**Figure S2**). As absolute intensities of XPS peaks can vary across samples, we opted to calculate and obtain an average area under graph ratio across 3 probe points within the same sample and compare those ratios across samples.

To obtain the relative surface terminations for  $-\text{F}_x$ ,  $-\text{O}_x$ , and  $-(\text{OH})_x$ , the area under graph ratios of  $\text{C}-\text{M}-\text{F}_x$ ,  $\text{C}-\text{M}-\text{O}_x$ , and  $\text{C}-\text{M}-\text{OH}_x$  of F 1s and O 1s spectra were calculated against the  $\text{C}-\text{M}-\text{T}_x$  deconvoluted peak area of C 1s spectrum, where M denotes the respective transition metal atoms found in the MXenes (**Figure 2c**).<sup>47</sup> This gives rise to ratios of 1.31, 0.474, and 1.38 respectively on  $\text{Mo}_2\text{Ti}_2\text{C}_3\text{T}_x$  MXene film, and ratios of 1.81, 0.258, and 0.249 respectively on  $\text{Ti}_3\text{C}_2\text{T}_x$  MXene film. Based on these ratios, it can be determined that the  $\text{Mo}_2\text{Ti}_2\text{C}_3\text{T}_x$  MXene has lesser  $-\text{F}_x$  terminations than  $\text{Ti}_3\text{C}_2\text{T}_x$  MXene but higher amounts of  $-\text{O}_x$ , and  $-(\text{OH})_x$  terminations than  $\text{Ti}_3\text{C}_2\text{T}_x$  MXene. Further results calculated from the atomic content obtained via XPS also corroborated with the above observation (**Figure 2d**), with the F/M atomic content ratio being higher in  $\text{Ti}_3\text{C}_2\text{T}_x$  MXene than  $\text{Mo}_2\text{Ti}_2\text{C}_3\text{T}_x$  MXene, and vice versa for the O/M ratios, highlighting the differences in surface terminations across both MXenes. Zeta-potentials of the MXene films when redispersed in water from their films at the same mass concentration were also obtained.  $\text{Mo}_2\text{Ti}_2\text{C}_3\text{T}_x$  MXene was observed to have a more

negative zeta potential of -41.8 mV than the -35.6 mV zeta potential of  $\text{Ti}_3\text{C}_2\text{T}_x$  MXenes (**Figure 2e**). This indicates that the  $\text{Mo}_2\text{Ti}_2\text{C}_3\text{T}_x$  MXene has a stronger charge density than  $\text{Ti}_3\text{C}_2\text{T}_x$  MXene and can potentially adsorb or desorb electrolyte species to a greater extent, allowing us to gain better insights through further analyses.

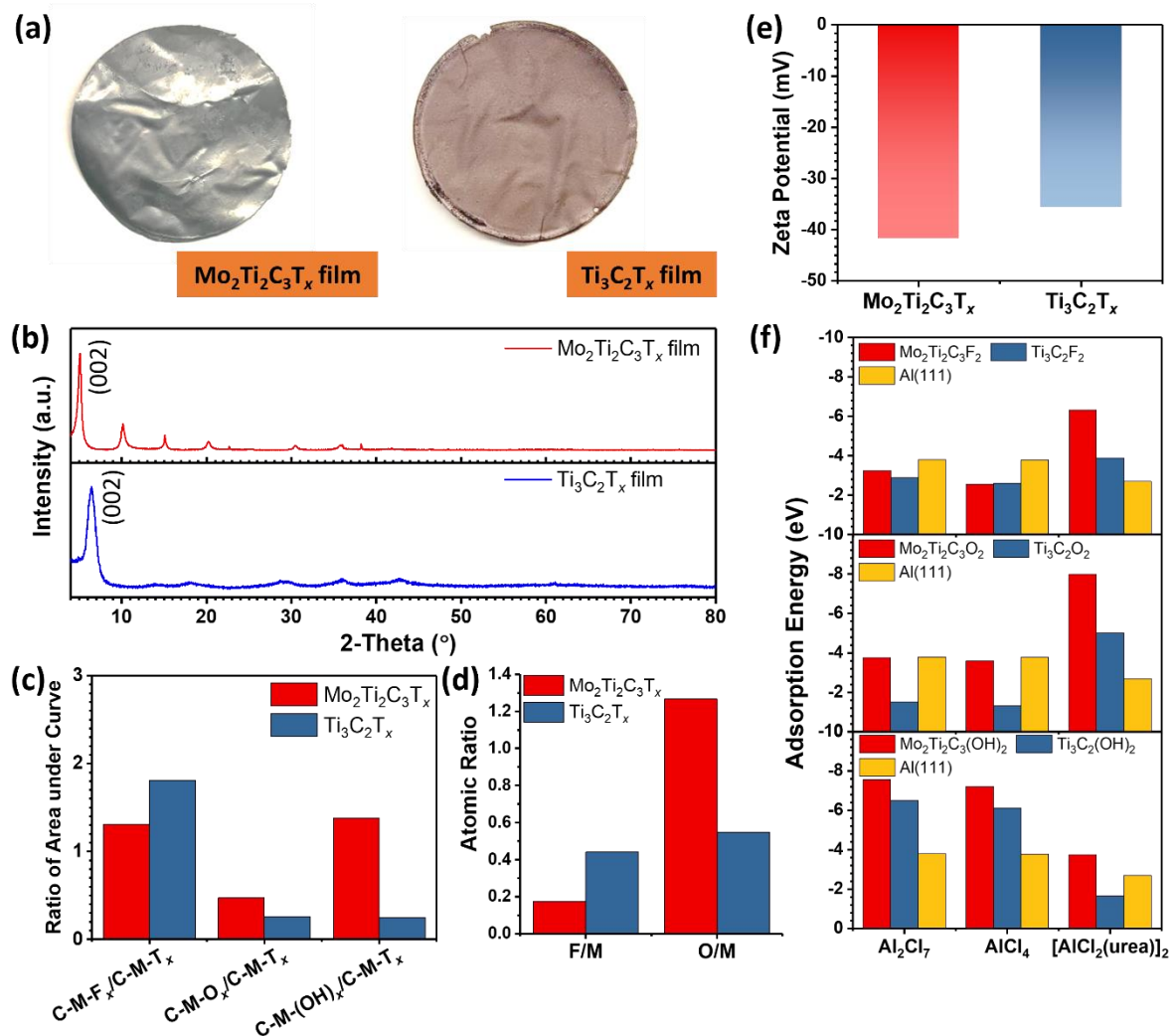


**Figure 2.** (a) Optical images and (b) XRD patterns of  $\text{Mo}_2\text{Ti}_2\text{C}_3\text{T}_x$  and  $\text{Ti}_3\text{C}_2\text{T}_x$  MXene films. (c) Comparison of surface termination ratios on  $\text{Mo}_2\text{Ti}_2\text{C}_3\text{T}_x$  and  $\text{Ti}_3\text{C}_2\text{T}_x$  MXenes through XPS deconvolution. M denotes the metal atoms (i.e., Ti and/or Mo). (d) Comparison of atomic ratios of fluorine and oxygen on  $\text{Mo}_2\text{Ti}_2\text{C}_3\text{T}_x$  and  $\text{Ti}_3\text{C}_2\text{T}_x$  MXenes averaged from 3 different probe points. M denotes the total metal percentage content (i.e., Ti and/or Mo). (e) Zeta-potential measurements of  $\text{Mo}_2\text{Ti}_2\text{C}_3\text{T}_x$  and  $\text{Ti}_3\text{C}_2\text{T}_x$  MXenes in water. (f) Adsorption energies of uncharged  $\text{Al}_2\text{Cl}_7$ ,  $\text{AlCl}_4$ , and  $[\text{AlCl}_2(\text{urea})_2]$  molecules on  $\text{Al}(111)$  surface and on different MXene surfaces.

Given that charge transfer occurs during the plating and stripping processes, we assume that  $\text{Al}_2\text{Cl}_7^-$  and  $[\text{AlCl}_2(\text{urea})_2]^+$  ions gain electrons and adsorb on the MXene electrode while  $\text{AlCl}_4^-$  ions lose electrons during the discharge or the Al plating process, and vice versa.<sup>48</sup> Density Functional Theory (DFT) calculations were hence conducted for the affinities of the

simplified, chargeless  $\text{AlCl}_4$ ,  $\text{Al}_2\text{Cl}_7$ , and  $[\text{AlCl}_2 \cdot (\text{urea})_2]$  molecules on the surfaces of  $\text{Al}(111)$  and MXenes with  $-\text{O}_x$ ,  $-(\text{OH})_x$ , and  $-\text{F}_x$  terminations (**Figure S3**). Adsorption energies of the molecules were calculated on the (111) surface of Al due to its known abundance in pure Al metal. Besides, previous research has also noted that Al metal preferentially forms (111) crystal facets during plating,<sup>49,50</sup> allowing the  $\text{Al}(111)$  facet to potentially serve as a benchmark. By taking into account the  $\text{Al}(111)$  facet, it is anticipated that there are 3 possible Al deposition morphologies for the following respective instances: when the Al surface has a better affinity towards the Al plating ions than the MXene surface; when the MXene surface has a better affinity to the ions than the Al surface; and when the MXene surface has similar affinities to the ions as compared to Al surface (**Figure S4**).

In general, the  $\text{Mo}_2\text{Ti}_2\text{C}_3\text{T}_x$  MXene mostly demonstrated higher adsorption energies compared to  $\text{Ti}_3\text{C}_2\text{T}_x$  MXene towards the Al-containing ions, except for  $\text{Mo}_2\text{Ti}_2\text{C}_3\text{F}_x$ , which showed slightly lower theoretical adsorption energy than  $\text{Ti}_3\text{C}_2\text{F}_x$  during the adsorption of  $\text{AlCl}_4$  (**Figure 2f**). Furthermore, if a pure  $\text{Mo}_2\text{Ti}_2\text{C}_3\text{F}_x$  MXene is present,  $\text{Al}_2\text{Cl}_7$  will be slightly preferentially adsorbed on the  $\text{Al}(111)$  face instead of the MXene. This is in contrast with  $[\text{AlCl}_2 \cdot (\text{urea})_2]$ , which shows greater adsorption energy with  $\text{Mo}_2\text{Ti}_2\text{C}_3\text{F}_x$  than  $\text{Al}(111)$ , potentially indicating that  $\text{Mo}_2\text{Ti}_2\text{C}_3\text{F}_x$  MXene is at a disadvantage compared to Al metal when plating is conducted in  $\text{EMImCl}/\text{AlCl}_3$ , but potentially vice versa in  $\text{urea}/\text{AlCl}_3$ . This is also similar for  $\text{Ti}_3\text{C}_2\text{F}_x$ , except to a smaller extent. Hence, this shows that both  $\text{Mo}_2\text{Ti}_2\text{C}_3\text{F}_x$  and  $\text{Ti}_3\text{C}_2\text{F}_x$  might perform better in  $\text{urea}/\text{AlCl}_3$  than in  $\text{EMImCl}/\text{AlCl}_3$ , although they are all unlikely to perform better than the  $\text{Al}(111)$  surface.

When the  $-\text{O}_x$  terminations of  $\text{Mo}_2\text{Ti}_2\text{C}_3\text{T}_x$  MXene film are considered, our calculations show that  $\text{Al}_2\text{Cl}_7$  can migrate to both the MXene and the  $\text{Al}(111)$  surfaces with similar preference, but  $[\text{AlCl}_2 \cdot (\text{urea})_2]$  is more likely to migrate towards the MXene surface. This is different from  $\text{Ti}_3\text{C}_2\text{O}_x$ , in which  $\text{Al}_2\text{Cl}_7$  and  $[\text{AlCl}_2 \cdot (\text{urea})_2]$  have potentially distinct preferences towards being adsorbed on  $\text{Al}(111)$  and  $\text{Ti}_3\text{C}_2\text{O}_x$  respectively. This shows that both  $-\text{O}_x$  terminated MXenes are likely to perform better in  $\text{urea}/\text{AlCl}_3$  than in  $\text{EMImCl}/\text{AlCl}_3$ , with the  $\text{Mo}_2\text{Ti}_2\text{C}_3\text{O}_x$  in  $\text{urea}/\text{AlCl}_3$  potentially better than  $\text{Al}(111)$ . Finally, the  $-(\text{OH})_x$  terminated MXenes have higher overall adsorption energies towards  $\text{Al}_2\text{Cl}_7$  and  $\text{Al}_2\text{Cl}_4$ , and lower adsorption energies towards  $[\text{AlCl}_2 \cdot (\text{urea})_2]$  as compared to the other terminations. On  $\text{Mo}_2\text{Ti}_2\text{C}_3(\text{OH})_x$  surface, both  $\text{Al}_2\text{Cl}_7$  and  $[\text{AlCl}_2 \cdot (\text{urea})_2]$  molecules might preferentially adsorb on MXene than  $\text{Al}(111)$ , whereas in  $\text{Ti}_3\text{C}_2(\text{OH})_x$ ,  $\text{Al}_2\text{Cl}_7$  might preferentially adsorb on MXene but  $[\text{AlCl}_2 \cdot (\text{urea})_2]$  might be preferentially adsorbed on  $\text{Al}(111)$ . This means that if a highly  $-(\text{OH})_x$ -saturated  $\text{Mo}_2\text{Ti}_2\text{C}_3\text{T}_x$

is obtained, it is likely to perform well in both urea/  $\text{AlCl}_3$  and EMImCl/ $\text{AlCl}_3$  electrolytes, better than Al(111). However, for the  $\text{Ti}_3\text{C}_2(\text{OH})_x$  MXene, it is likely to undergo plating better in EMImCl/ $\text{AlCl}_3$  than in urea/ $\text{AlCl}_3$ , with the urea/ $\text{AlCl}_3$  system potentially being subpar in comparison with Al(111). The above analysis is summarised in **Table S1** for easy reference.

Nonetheless, the above analysis is a simplified method to deduce a potentially good theoretical host for RABs. In actual RABs, Al stripping needs to be considered as well and this might be promoted by low adsorption energies of  $\text{AlCl}_4^-$  ions. Based on the conducted adsorption energy calculations, the adsorption energies of  $\text{AlCl}_4$  molecules on surfaces are close to that of  $\text{Al}_2\text{Cl}_7$ . Hence, it might not be easy to determine both Al plating and stripping characteristics solely from the above adsorption energy calculations.

### Al deposition in Urea/AlCl<sub>3</sub> electrolyte

Al deposition was conducted at a current density of 0.25 mA/cm<sup>2</sup> and an areal capacity of 0.25 mAh/cm<sup>2</sup> on Mo<sub>2</sub>Ti<sub>2</sub>C<sub>3</sub>T<sub>x</sub> and Ti<sub>3</sub>C<sub>2</sub>T<sub>x</sub> MXenes using the urea/AlCl<sub>3</sub> electrolyte in a Swagelok cell to minimise corrosion. The resultant MXene films were washed using anhydrous dimethyl carbonate (DMC).<sup>51</sup> Based on the scanning electron microscopy (SEM) images and the corresponding energy dispersive X-ray spectroscopy (EDS) maps in **Figure 3a**, both MXene surfaces were observed to have an additional Al-containing layer covering the original MXene layer. Cyclic voltammetry (CV) tests were also conducted at 1 mV/s to determine the Al plating and stripping capabilities of the two MXenes (**Figure 3b**). A typical redox couple corresponding to Al plating (reduction) and stripping (oxidation) was observed in the voltage range of -0.4 V to 0.9 V versus Al/Al<sup>3+</sup>, with peaks potentially indicating the presence of side reactions on the Mo<sub>2</sub>Ti<sub>2</sub>C<sub>3</sub>T<sub>x</sub> MXene film. The consistent CV curves from the 2<sup>nd</sup> cycle to the 6<sup>th</sup> cycle for both MXenes also showed that Al plating/stripping is reversible when the urea/AlCl<sub>3</sub> electrolyte was used (**Figure S5**).

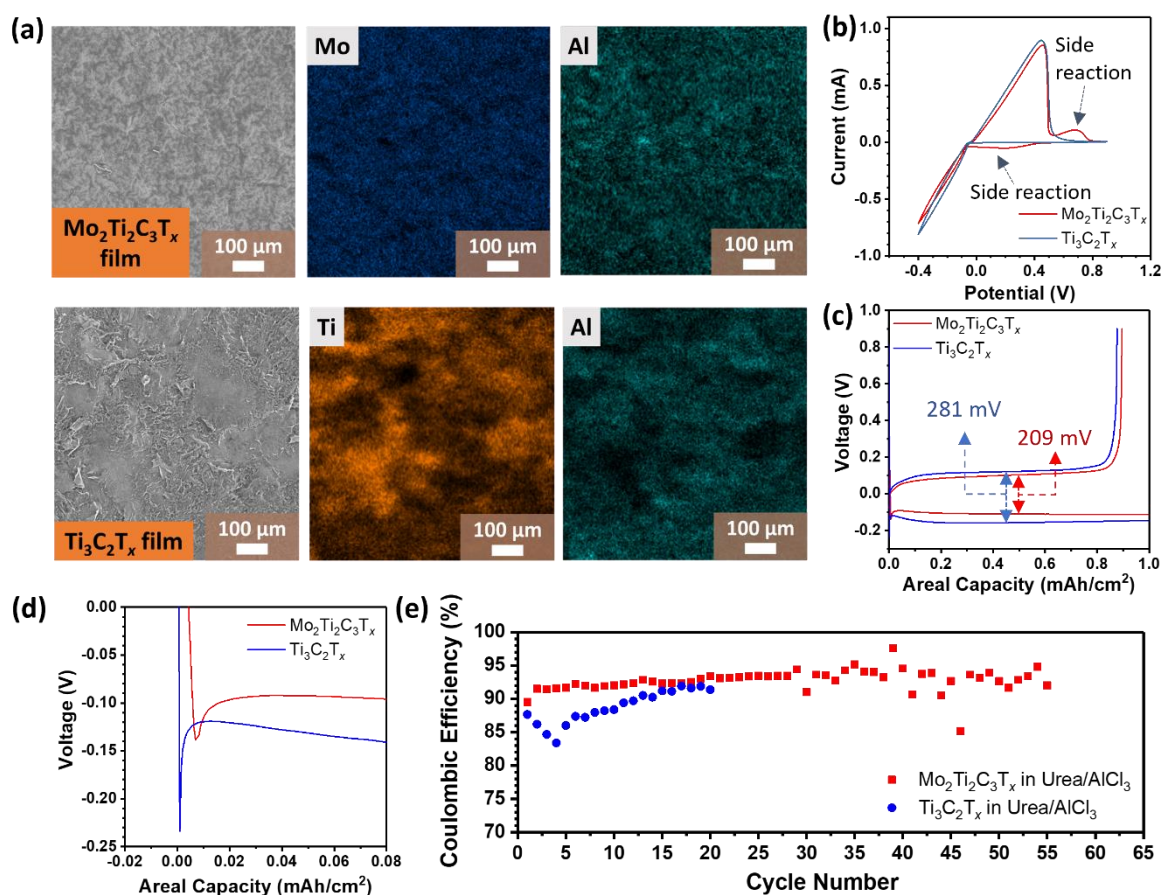


**Figure 3.** (a) SEM images and EDS mapping of MXenes after 0.25 mAh/cm<sup>2</sup> of Al plating capacity at a current rate of 0.25 mA/cm<sup>2</sup> in urea/AlCl<sub>3</sub> electrolyte. (b) 5<sup>th</sup> CV cycle demonstrating the Al plating and stripping

capabilities of both MXenes. (c) Voltage hysteresis of the first discharge-charge cycle, (d) nucleation overpotentials of the first discharge curve, and (e) coulombic efficiencies of both  $\text{Mo}_2\text{Ti}_2\text{C}_3\text{T}_x$  and  $\text{Ti}_3\text{C}_2\text{T}_x$  films at a current rate of  $0.5 \text{ mA/cm}^2$  and an Al plating capacity of  $1 \text{ mAh/cm}^2$ .

The first discharge and charge plateaus of  $\text{Mo}_2\text{Ti}_2\text{C}_3\text{T}_x$  MXene were observed to have a smaller voltage hysteresis of  $209 \text{ mV}$  than  $281 \text{ mV}$  in  $\text{Ti}_3\text{C}_2\text{T}_x$  MXene (**Figure 3c**). A similar trend was also observed in the nucleation overpotential values, where the  $\text{Mo}_2\text{Ti}_2\text{C}_3\text{T}_x$  MXene was observed to have a lower nucleation overpotential of  $39 \text{ mV}$  as compared to  $\text{Ti}_3\text{C}_2\text{T}_x$ 's  $112 \text{ mV}$  (**Figure 3d**). The plating/stripping coulombic efficiencies (CE) of the MXenes were also calculated at a current density of  $0.5 \text{ mA/cm}^2$  and an areal capacity of  $1 \text{ mAh/cm}^2$  (**Figure 3e**). It is shown that  $\text{Mo}_2\text{Ti}_2\text{C}_3\text{T}_x$  film in the urea/ $\text{AlCl}_3$  electrolyte had a higher average CE value of  $92.7 \%$  and was able to conduct plating and stripping for 55 cycles before shorting, whereas  $\text{Ti}_3\text{C}_2\text{T}_x$  had a lower CE value of  $88.8 \%$  and shorted after 20 cycles, thus indicating that the  $\text{Mo}_2\text{Ti}_2\text{C}_3\text{T}_x$  MXene performed better in the urea/ $\text{AlCl}_3$  electrolyte. **Similar CE experiments were also conducted at  $1 \text{ mA/cm}^2$  and  $1 \text{ mAh/cm}^2$  for  $\text{Mo}_2\text{Ti}_2\text{C}_3\text{T}_x$  MXene film and  $\text{Ti}_3\text{C}_2\text{T}_x$  MXene film, giving average CEs of  $96.1 \%$  and  $93.3 \%$  respectively, with a cycling life of 10 cycles or less for both films (**Figure S6**). Further control experiments using Mo foil and carbon paper were also performed at  $0.5 \text{ mA/cm}^2$  and  $1 \text{ mAh/cm}^2$  current density and areal capacity in the urea/ $\text{AlCl}_3$  electrolyte (**Figure S7**), with both showing consistent CV curves, short cycling lives and an average CE of  $79.7\%$  and  $89.3\%$  respectively.**

Thereafter, XPS was conducted to further identify the chemical species on the Al-deposited films.  $\text{Ar}^+$  ion sputtering was conducted for 60 min and XPS spectra were obtained for each Al-deposited MXene at intervals of 0 s and 60 min (**Figure 4a, b, S8**). Based on the Al 2p spectra, at the 60-minute interval, it was observed that both  $\text{Mo}_2\text{Ti}_2\text{C}_3\text{T}_x$  and  $\text{Ti}_3\text{C}_2\text{T}_x$  MXene had Al metal peaks. The Al-deposited  $\text{Mo}_2\text{Ti}_2\text{C}_3\text{T}_x$  also had an additional peak assigned to  $\text{Al}_2\text{O}_3$  in the O 1s spectrum, which might be an indication that the amount of Al successfully plated on the  $\text{Mo}_2\text{Ti}_2\text{C}_3\text{T}_x$  film, and thereafter oxidised, might be larger than the  $\text{Ti}_3\text{C}_2\text{T}_x$  film. One main difference between the XPS spectra of the  $\text{Mo}_2\text{Ti}_2\text{C}_3\text{T}_x$  and  $\text{Ti}_3\text{C}_2\text{T}_x$  MXenes is that after etching for 60 min, Al-F peaks were observed in the Al 2p spectra of Al-deposited  $\text{Ti}_3\text{C}_2\text{T}_x$  MXene film, whereas only a small Al-F peak was observed on Al-deposited  $\text{Mo}_2\text{Ti}_2\text{C}_3\text{T}_x$  MXene film. These results were further corroborated by the F 1s spectra of the Al-deposited  $\text{Mo}_2\text{Ti}_2\text{C}_3\text{T}_x$  and  $\text{Ti}_3\text{C}_2\text{T}_x$  MXenes films. After 60 min of  $\text{Ar}^+$  ion etching, peaks belonging to the  $\text{AlF}_x$  and  $\text{Al}(\text{OF})_x$  species were observed along with the C-Ti-F<sub>x</sub> (III) peak of  $\text{Ti}_3\text{C}_2\text{T}_x$  MXene. However, the F 1s spectrum of  $\text{Mo}_2\text{Ti}_2\text{C}_3\text{T}_x$  MXene after etching for 60 min could not be further

deconvoluted, indicating the absence of those species. This might be due to the relatively lower amounts of  $-F$  terminations present on the  $\text{Mo}_2\text{Ti}_2\text{C}_3\text{T}_x$  MXene film, resulting in lesser  $\text{AlF}_x$  and  $\text{Al}(\text{OF})_x$  species being formed.

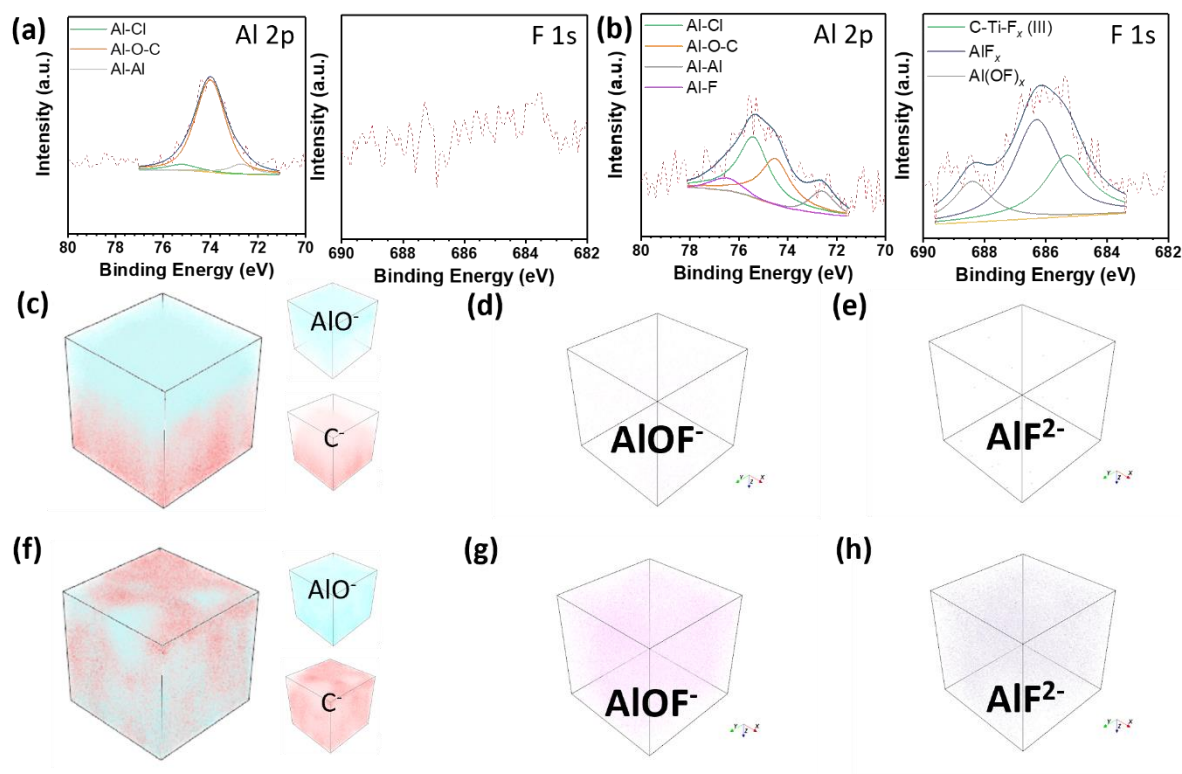


**Figure 4.** Al 2p and F 1s spectra of (a)  $\text{Mo}_2\text{Ti}_2\text{C}_3\text{T}_x$  and (b)  $\text{Ti}_3\text{C}_2\text{T}_x$  MXene films after  $\text{Ar}^+$  ion etching for 60 min. ToF-SIMS 3D maps (depth 400 nm, area of  $50\ \mu\text{m}$  by  $50\ \mu\text{m}$ ) of  $\text{Mo}_2\text{Ti}_2\text{C}_3\text{T}_x$  MXene film after Al deposition for (c) the overlaps of  $\text{AlO}^-$  and  $\text{C}^-$  ions, the (d)  $\text{AlOF}^-$  ions, and the (e)  $\text{AlF}^{2-}$  ions. Equivalent 3D maps were also obtained for  $\text{Ti}_3\text{C}_2\text{T}_x$  MXene film after Al deposition for (f) the overlaps of  $\text{AlO}^-$  and  $\text{C}^-$  ions, the (g)  $\text{AlOF}^-$  ions, and the (h)  $\text{AlF}^{2-}$  ions

Time-of-flight secondary ion mass spectrometry (ToF-SIMS) was also conducted to determine the chemical compositions of the MXenes after Al deposition. After Al-deposition on  $\text{Mo}_2\text{Ti}_2\text{C}_3\text{T}_x$  MXene in urea/ $\text{AlCl}_3$ , a layer of  $\text{AlO}^-$  ions was observed to form above a layer of  $\text{C}^-$  ions (**Figure 4c**). This contrasts with the ToF-SIMS map obtained from the Al-deposited  $\text{Ti}_3\text{C}_2\text{T}_x$  film, where distinct layers were not observed between  $\text{AlO}^-$  and  $\text{C}^-$  layers (**Figure 4f**). Besides the cross-sectional visualisation of Al, TOF-SIMS could also be used to visualise the relative amounts of  $\text{Al}(\text{OF})_x$  and  $\text{AlF}_x$  available after Al deposition. As shown in **Figure 4d, e and 4g, h** respectively, the Al-deposited  $\text{Mo}_2\text{Ti}_2\text{C}_3\text{T}_x$  MXene film produced 3D maps with lower intensities of  $\text{AlOF}^-$  and  $\text{AlF}^{2-}$  ions compared to the  $\text{Ti}_3\text{C}_2\text{T}_x$  film. This potentially indicates that  $\text{Al}(\text{OF})_x$  and  $\text{AlF}_x$  species are formed due to an interfacial reaction between the

Al<sub>2</sub>O<sub>3</sub> (or the Al metal) and the –F terminations of MXene, indicating the occurrence of side reactions.

The (00 $l$ ) XRD peak positions of the Al-deposited Mo<sub>2</sub>Ti<sub>2</sub>C<sub>3</sub>T <sub>$x$</sub>  MXene film did not change after both Al plating and stripping even though the intensity of the (002) peak decreased significantly in comparison with the other (00 $l$ ) peaks. Instead, a new Al(111) XRD peak at 38.3° was observed after Al plating (PDF no. 04-0787), which thereafter disappeared with Al stripping (**Figure 5a**), further serving as evidence of Al metal deposition. This contrasts with the XRD pattern of Al-deposited Ti<sub>3</sub>C<sub>2</sub>T <sub>$x$</sub>  MXene film, which did not consist of new Al peaks (**Figure S9**). Furthermore, no shift in the 2-theta position of the Ti<sub>3</sub>C<sub>2</sub>T <sub>$x$</sub> 's (002) peak was observed after both Al plating and stripping, indicating the absence of change in MXene interlayer spacing (**Figure 5b**). Thereafter, MXene films that were deposited with Al at a current density of 0.1 mA/cm<sup>2</sup> and an areal capacity of 0.1 mAh/cm<sup>2</sup> were washed with DMC and further dispersed in ethanol for TEM imaging.<sup>43</sup> Based on the obtained TEM images, both Al and Al<sub>2</sub>O<sub>3</sub> particles, the latter which could have arisen from oxidation, were observed on the 2D MXene sheets in **Figure 5c, d, and e** when deposited on Mo<sub>2</sub>Ti<sub>2</sub>C<sub>3</sub>T <sub>$x$</sub>  and Ti<sub>3</sub>C<sub>2</sub>T <sub>$x$</sub>  MXenes. Lattice spacings of approximately 2.3 Å, 2.0 Å, and 2.5 Å were observed to correspond to Al(111), Al(200), and Al<sub>2</sub>O<sub>3</sub>(104) respectively and further SAED images also demonstrated the crystalline nature of the particles deposited (**Figure S10**).

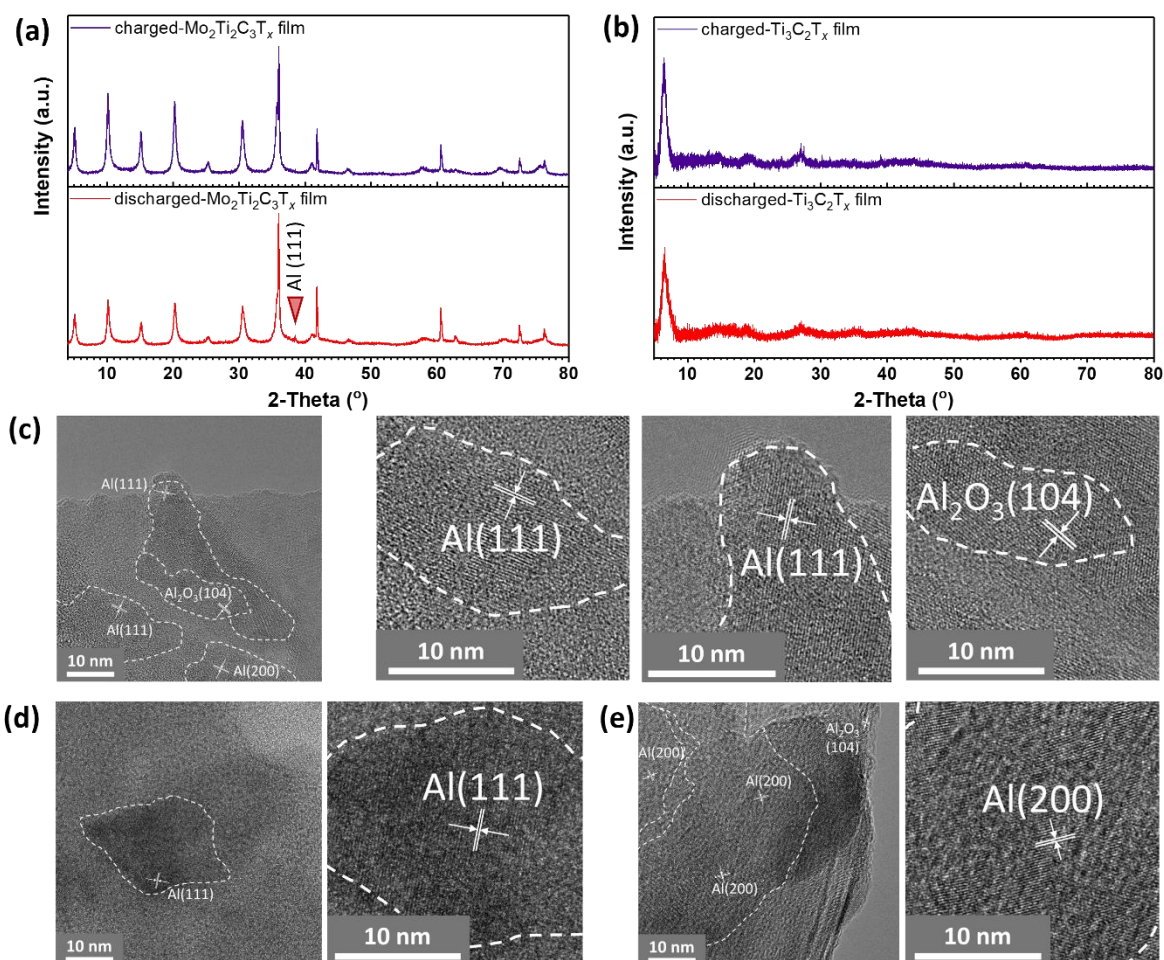


**Figure 5.** XRD patterns of (a)  $\text{Mo}_2\text{Ti}_2\text{C}_3\text{T}_x$  and (b)  $\text{Ti}_3\text{C}_2\text{T}_x$  MXene films after discharge and charge at a current density of  $0.5 \text{ mA/cm}^2$ , and a capacity of  $0.5 \text{ mAh/cm}^2$ . TEM images of (c)  $\text{Mo}_2\text{Ti}_2\text{C}_3\text{T}_x$  and (d, e)  $\text{Ti}_3\text{C}_2\text{T}_x$  MXene films after Al deposition at an areal current density of  $0.1 \text{ mA/cm}^2$  and an areal capacity of  $0.1 \text{ mAh/cm}^2$ .

To further study the morphology of Al-deposited MXenes, SEM images of Al-deposited MXenes at areal capacities of  $1 \text{ mAh/cm}^2$ ,  $2 \text{ mAh/cm}^2$ ,  $4 \text{ mAh/cm}^2$ , and  $8 \text{ mAh/cm}^2$  were also taken and compared with pre-deposited MXene films (**Figure S11, S12a**). At  $1 \text{ mAh/cm}^2$ , the Al crystals were deposited on both MXenes in a conformal layer with a compact microparticulate structure without significant signs of aggressive and/or dendritic growth. However, at higher areal capacities of above  $2 \text{ mAh/cm}^2$ , the Al-deposited  $\text{Ti}_3\text{C}_2\text{T}_x$  MXene had a significantly more uneven surface morphology as compared to its  $\text{Mo}_2\text{Ti}_2\text{C}_3\text{T}_x$  MXene counterpart, which might be an indication that Al deposition is enhanced on  $\text{Mo}_2\text{Ti}_2\text{C}_3\text{T}_x$  in the urea/ $\text{AlCl}_3$  electrolyte. Aggressive particulate growth and cracks were observed on both  $\text{Mo}_2\text{Ti}_2\text{C}_3\text{T}_x$  and  $\text{Ti}_3\text{C}_2\text{T}_x$  MXene after depositing Al at an areal capacity of  $8 \text{ mAh/cm}^2$ , indicating the structural limitations of the MXene vacuum-filtrated freestanding film. SEM images were also taken at higher magnitudes, revealing that while the Al deposits looked like

distinct microparticles macroscopically, distinct microparticle edges are not as apparent (**Figure S12b**). This is particularly observed in the Al-deposited  $\text{Mo}_2\text{Ti}_2\text{C}_3\text{T}_x$  MXene film, in which vague edges of the microparticles were only observed at  $4 \text{ mAh/cm}^2$ . Overall, XPS, ToF-SIMS, XRD and microscopic analysis is hinting that Al electrodeposition in urea/ $\text{AlCl}_3$  is much uniform and controlled on  $\text{Mo}_2\text{Ti}_2\text{C}_3\text{T}_x$  MXene as compared to the  $\text{Ti}_3\text{C}_2\text{T}_x$  MXene, which also gets reflected in the electrochemical study in terms of cycling life and CE.

### Al deposition in EMImCl/AlCl<sub>3</sub> electrolyte

Similarly, Al was also deposited at a current density of 0.5 mA/cm<sup>2</sup> and an areal capacity of 0.5 mAh/cm<sup>2</sup> on both Mo<sub>2</sub>Ti<sub>2</sub>C<sub>3</sub>T<sub>x</sub> and Ti<sub>3</sub>C<sub>2</sub>T<sub>x</sub> MXenes using the EMImCl/AlCl<sub>3</sub> electrolyte in a Swagelok cell and thereafter washed with anhydrous DMC. In comparison with the urea/AlCl<sub>3</sub> electrolyte, Al deposition in the EMImCl/AlCl<sub>3</sub> electrolyte generates a surface morphology with greater irregularity. According to the SEM and EDS maps, obvious Al microparticles were observed from the Mo<sub>2</sub>Ti<sub>2</sub>C<sub>3</sub>T<sub>x</sub> MXene film across a large area, whereas small clumps were observed on the Ti<sub>3</sub>C<sub>2</sub>T<sub>x</sub> MXene film (**Figure 6a**). CV curves at a rate of 1 mV/s also reveal that Al plating and stripping can occur on both MXenes at -0.4 V to 0.9 V versus Al/Al<sup>3+</sup> (**Figure 6b**). Like the CV curves obtained in the urea/AlCl<sub>3</sub> electrolyte, peaks likely belonging to side reactions were observed when the Mo<sub>2</sub>Ti<sub>2</sub>C<sub>3</sub>T<sub>x</sub> MXene was used. However, differing from the urea/AlCl<sub>3</sub> electrolyte results, the EMImCl/AlCl<sub>3</sub> electrolyte showed that the peak current values approximately quadrupled for both MXenes. **Furthermore, although the CV curves of Mo<sub>2</sub>Ti<sub>2</sub>C<sub>3</sub>T<sub>x</sub> MXene remained consistent, inconsistent CV curves were observed after repeated plating and stripping of Al metal on the Ti<sub>3</sub>C<sub>2</sub>T<sub>x</sub> MXene film (Figure S13), which might be evidence that the redox process is not entirely reversible throughout the discharge/charge cycles. This might be attributed to unknown side reactions that have an oxidation potential close to the oxidation potential of Al/Al<sup>3+</sup>, resulting in inconsistent CV curves.**

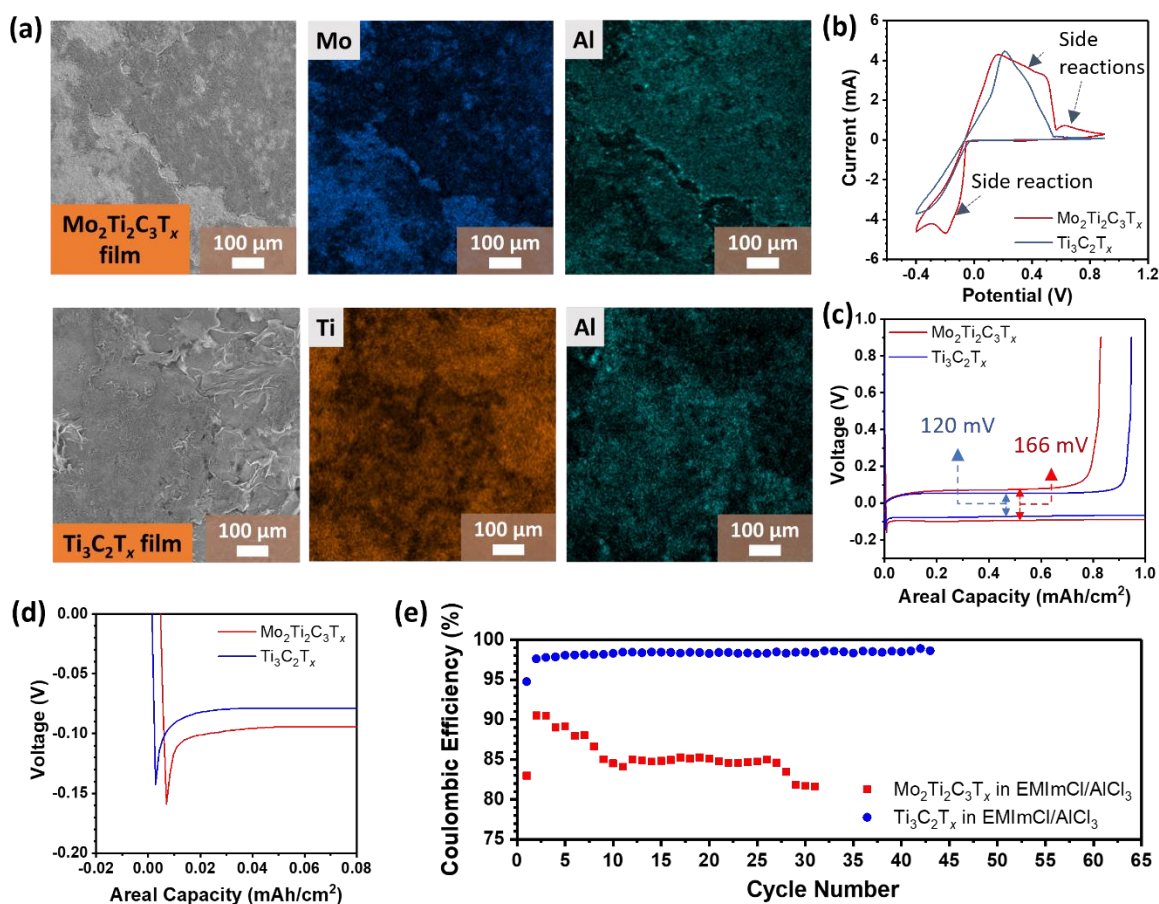


**Figure 6.** (a) SEM images and EDS mapping of MXenes after 0.25 mAh/cm<sup>2</sup> of Al plating capacity at a current rate of 0.25 mA/cm<sup>2</sup> in EMImCl/AlCl<sub>3</sub> electrolyte. (b) 5<sup>th</sup> CV cycle demonstrating the Al plating and stripping capabilities of both MXenes. (c) Voltage hysteresis of the first discharge-charge cycle, (d) nucleation overpotentials of the first discharge curve, and (e) coulombic efficiencies of both  $\text{Mo}_2\text{Ti}_2\text{C}_3\text{T}_x$  and  $\text{Ti}_3\text{C}_2\text{T}_x$  films at a current rate of 0.5 mA/cm<sup>2</sup> and an Al plating capacity of 1 mAh/cm<sup>2</sup>.

Unlike the urea/AlCl<sub>3</sub> electrolyte, the first discharge and charge cycle of  $\text{Ti}_3\text{C}_2\text{T}_x$  MXene was shown to have a smaller voltage hysteresis of 120 mV than 166 mV in  $\text{Mo}_2\text{Ti}_2\text{C}_3\text{T}_x$  MXene (**Figure 6c**), while similar nucleation overpotential values of 61.3 mV and 58.8 mV were observed for  $\text{Ti}_3\text{C}_2\text{T}_x$  and  $\text{Mo}_2\text{Ti}_2\text{C}_3\text{T}_x$  MXenes respectively (**Figure 6d**). The plating/stripping CE of the MXenes was also measured at a current density of 0.5 mA/cm<sup>2</sup> and an areal capacity of 1 mAh/cm<sup>2</sup> (**Figure 6e**). It was observed that the  $\text{Ti}_3\text{C}_2\text{T}_x$  MXene had a higher average CE of 98.3 % and a cycle life of 43 cycles, while the  $\text{Mo}_2\text{Ti}_2\text{C}_3\text{T}_x$  MXene had a decreasing CE with an average CE of 85.3 % and a cycle life of 31 cycles. This shows that opposite to the urea/AlCl<sub>3</sub> electrolyte,  $\text{Ti}_3\text{C}_2\text{T}_x$  MXene performs plating and stripping better in the EMImCl/AlCl<sub>3</sub> electrolyte as compared to the  $\text{Mo}_2\text{Ti}_2\text{C}_3\text{T}_x$  MXene, highlighting that a generic rule does not necessarily apply for all electrolytes of the RAB system. **CE experiments were also conducted at 1 mA/cm<sup>2</sup> and 1 mAh/cm<sup>2</sup> for  $\text{Mo}_2\text{Ti}_2\text{C}_3\text{T}_x$  MXene film and  $\text{Ti}_3\text{C}_2\text{T}_x$  MXene**

film, giving average CEs of 99.7 % and 99.0 % respectively (**Figure S14**). However, both MXene films had several occurrences where the CE value exceeded 100 %, potentially supporting our previous conjecture involving the prevalence of side reactions when the EMImCl/AlCl<sub>3</sub> electrolyte is used. Further control experiments using Mo foil and carbon paper were also performed at 0.5 mA/cm<sup>2</sup> and 1 mAh/cm<sup>2</sup> current density and areal capacity in the EMImCl/AlCl<sub>3</sub> electrolyte (**Figure S15**), demonstrating high average CE of 98.3 % and 99.5 % respectively. While such high CE values are commendable, the broadened anodic peaks and non-overlapping CV curves obtained CV curves demonstrate that both Mo foil and carbon paper are likely to undergo side reactions when used in the EMImCl/AlCl<sub>3</sub> electrolyte due to the increase in current amplitudes and consistent peak shifts as the cycle number increases, like that observed when the Ti<sub>3</sub>C<sub>2</sub>T<sub>x</sub> MXene film was used. This is particularly so when carbon paper is used as its CE values often went above 100 % during cycling, therefore giving a strong indication that the EMImCl/AlCl<sub>3</sub> electrolyte has a high tendency to result in the occurrence of side reactions.

XPS analyses were also conducted with Ar<sup>+</sup> ion etching at intervals of 0 s and 60 min (**Figure 7a, b, and S16**). Al metal peaks were observed on both Mo<sub>2</sub>Ti<sub>2</sub>C<sub>3</sub>T<sub>x</sub> and Ti<sub>3</sub>C<sub>2</sub>T<sub>x</sub> after 60 min of etching, indicating successful electrodeposition. Furthermore, differing from the urea/AlCl<sub>3</sub> electrolyte, Al<sub>2</sub>O<sub>3</sub> were already observed in the O 1s spectra of both Mo<sub>2</sub>Ti<sub>2</sub>C<sub>3</sub>T<sub>x</sub> and Ti<sub>3</sub>C<sub>2</sub>T<sub>x</sub> films prior to etching. This might be an indication that Al plating is more effective in the EMImCl/AlCl<sub>3</sub> system compared to urea/AlCl<sub>3</sub>. AlF<sub>x</sub> and Al(OH)<sub>x</sub> species were also observed via the F 1s spectra of both MXenes in varying amounts across different etch intervals. This is in stark contrast with the XPS results obtained using the urea/AlCl<sub>3</sub> electrolyte which showed that the Al-deposited Mo<sub>2</sub>Ti<sub>2</sub>C<sub>3</sub>T<sub>x</sub> had almost negligible amount of AlF<sub>x</sub> and Al(OH)<sub>x</sub> species available.

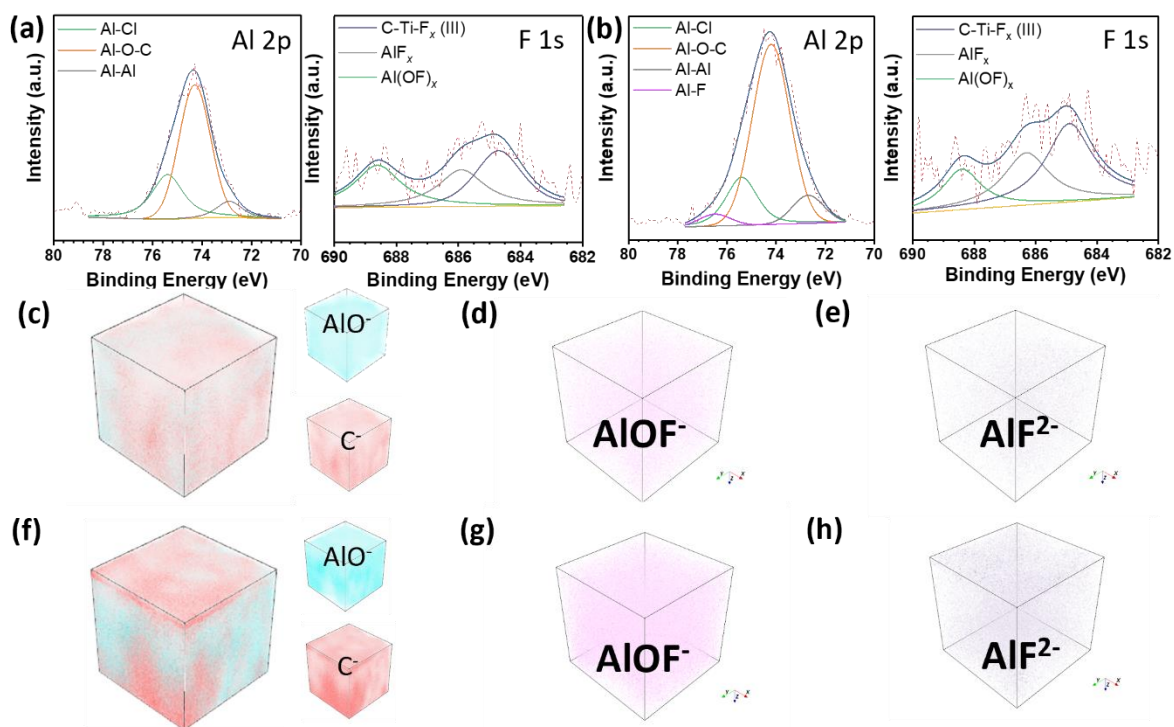


**Figure 7.** Al 2p and F1s spectra of **(a)**  $\text{Mo}_2\text{Ti}_2\text{C}_3\text{T}_x$  and **(b)**  $\text{Ti}_3\text{C}_2\text{T}_x$  film after  $\text{Ar}^+$  ion etching for 60 min. ToF-SIMS 3D maps of  $\text{Mo}_2\text{Ti}_2\text{C}_3\text{T}_x$  after Al deposition for **(c)** the overlaps of  $\text{AlO}^-$  and  $\text{C}^-$  ions, the **(d)**  $\text{AlOF}^-$  ions, and the **(e)**  $\text{AlF}^{2-}$  ions. Similar 3D maps were also obtained for  $\text{Ti}_3\text{C}_2\text{T}_x$  after Al deposition for **(f)** the overlaps of  $\text{AlO}^-$  and  $\text{C}^-$  ions, the **(g)**  $\text{AlOF}^-$  ions, and the **(h)**  $\text{AlF}^{2-}$  ions.

ToF-SIMS study with the same conditions as before also show contrasting observation from the urea/ $\text{AlCl}_3$  electrolyte system,  $\text{AlO}^-$  ions were not observed to form a distinct layer from  $\text{C}^-$  ions in the Al-deposited  $\text{Mo}_2\text{Ti}_2\text{C}_3\text{T}_x$  but were observed to form a distinct layer from  $\text{C}^-$  ions in the Al-deposited  $\text{Ti}_3\text{C}_2\text{T}_x$  film (**Figure 7c, f**). This agrees with the previous CV results, which showed that the  $\text{Mo}_2\text{Ti}_2\text{C}_3\text{T}_x$  MXene had much broader anodic peaks than  $\text{Ti}_3\text{C}_2\text{T}_x$  MXene films. Such broader peaks can indicate that the reaction is not a simple reversible redox process and can involve more electrochemical species than expected during plating and stripping, therefore affecting the effective amount of Al deposited on the  $\text{Mo}_2\text{Ti}_2\text{C}_3\text{T}_x$  MXene film. 3D maps of  $\text{AlOF}^-$  and  $\text{AlF}^{2-}$  also show that both Al-deposited  $\text{Mo}_2\text{Ti}_2\text{C}_3\text{T}_x$  and  $\text{Ti}_3\text{C}_2\text{T}_x$  MXene films had  $\text{Al}(\text{OF})_x$  and  $\text{AlF}_x$  throughout the first 400 nm depth from the surface of the two films, corroborating with the previous XPS results (**Figure 7 d, e, g, and h**). Nonetheless, the Al-deposited  $\text{Ti}_3\text{C}_2\text{T}_x$  MXene film has visibly higher amounts of  $\text{Al}(\text{OF})_x$  and  $\text{AlF}_x$  compared to the  $\text{Mo}_2\text{Ti}_2\text{C}_3\text{T}_x$  MXene film, indicating that the amount of  $-\text{F}$  terminations on the MXene surface still affects the extent of side reactions.

Further XRD was conducted on the Al-deposited  $\text{Mo}_2\text{Ti}_2\text{C}_3\text{T}_x$  and  $\text{Ti}_3\text{C}_2\text{T}_x$  MXene films. Unlike the urea/ $\text{AlCl}_3$  electrolyte system, no obvious Al metal peaks were observed in the XRD pattern of the  $\text{Mo}_2\text{Ti}_2\text{C}_3\text{T}_x$  MXene both after plating and stripping (**Figure 8a**). 2-theta positions of both  $\text{Mo}_2\text{Ti}_2\text{C}_3\text{T}_x$ 's (002) peak and  $\text{Ti}_3\text{C}_2\text{T}_x$ 's (002) peak were also not observed to shift significantly. However, new peaks were identified after Al plating  $\text{Ti}_3\text{C}_2\text{T}_x$  MXene at  $38.5^\circ$  and  $44.7^\circ$  (**Figure 8b**), corresponding to Al(111) and Al(200) peaks respectively. These peaks were subsequently not observed after the stripping of Al. Further smaller peaks were also observed, and to the best of our knowledge, we determined that they are not aluminium-containing species. TEM analyses were also conducted for the EMImCl/ $\text{AlCl}_3$  system, in which MXene films were deposited with Al at a current density of  $0.1 \text{ mA/cm}^2$  and an areal capacity of  $0.1 \text{ mAh/cm}^2$ , washed and further dispersed in ethanol. Like the urea/ $\text{AlCl}_3$  system, Al and  $\text{Al}_2\text{O}_3$  particles were observed on the 2D MXene sheets in **Figure 8c**, when deposited on  $\text{Mo}_2\text{Ti}_2\text{C}_3\text{T}_x$  and  $\text{Ti}_3\text{C}_2\text{T}_x$  respectively. The Al particles found on  $\text{Ti}_3\text{C}_2\text{T}_x$  were significantly larger as compared to  $\text{Mo}_2\text{Ti}_2\text{C}_3\text{T}_x$  (**Figure 8 d, e**). Nonetheless, as Al metal oxidises easily,  $\text{Al}_2\text{O}_3$  were also observed from the SAED images of  $\text{Ti}_3\text{C}_2\text{T}_x$ , like  $\text{Mo}_2\text{Ti}_2\text{C}_3\text{T}_x$  MXene (**Figure S17**).

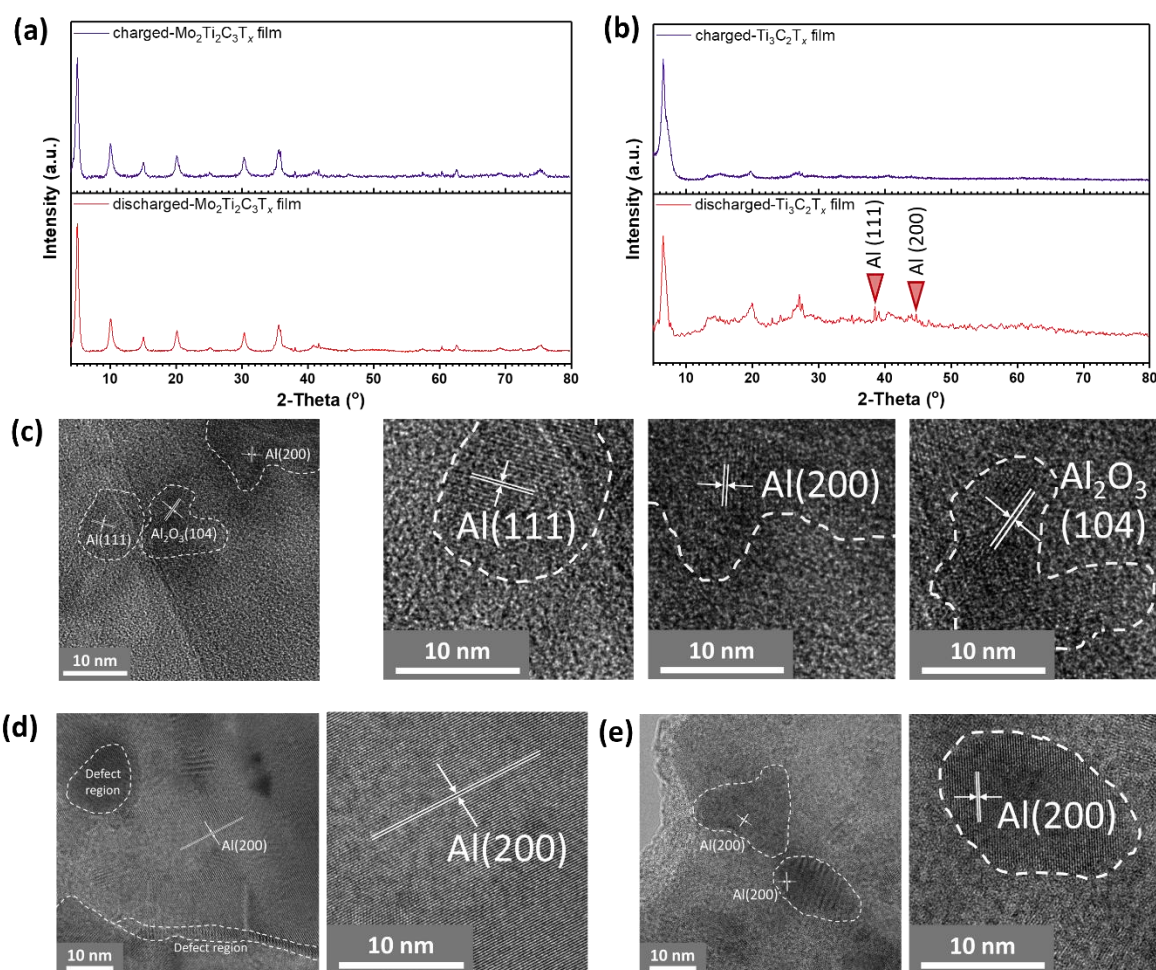


**Figure 8.** XRD patterns of (a)  $\text{Mo}_2\text{Ti}_2\text{C}_3\text{T}_x$  and (b)  $\text{Ti}_3\text{C}_2\text{T}_x$  films after discharge and charge at a current density of  $0.5 \text{ mA/cm}^2$ , and a capacity of  $0.5 \text{ mAh/cm}^2$ . TEM images of (c)  $\text{Mo}_2\text{Ti}_2\text{C}_3\text{T}_x$  and (d, e)  $\text{Ti}_3\text{C}_2\text{T}_x$  films after Al deposition at an areal current density of  $0.1 \text{ mA/cm}^2$  and an areal capacity of  $0.1 \text{ mAh/cm}^2$ .

SEM images of Al-deposited MXenes with areal capacities of  $1 \text{ mAh/cm}^2$ ,  $2 \text{ mAh/cm}^2$ ,  $4 \text{ mAh/cm}^2$ , and  $8 \text{ mAh/cm}^2$  were also taken (**Figure S18**). While  $\text{Ti}_3\text{C}_2\text{T}_x$  MXene retained the compact surface deposition morphology that was observed on both MXenes when in the urea/ $\text{AlCl}_3$  electrolyte system,  $\text{Mo}_2\text{Ti}_2\text{C}_3\text{T}_x$  showed very irregular surface texture. Large and distinct clumps of Al deposits were observed (**Figure S18a**). Hence, when the Al-deposited  $\text{Mo}_2\text{Ti}_2\text{C}_3\text{T}_x$  film was viewed macroscopically, there were a lot of pits on the surface, stemming from the deposited Al's inability to form a conformal surface. With higher areal capacities, this clumpy deposit formation eventually results in protruding surface structures (**Figure S18b**), particularly observed in the SEM images of  $4 \text{ mAh/cm}^2$  and  $8 \text{ mAh/cm}^2$  deposited  $\text{Mo}_2\text{Ti}_2\text{C}_3\text{T}_x$  MXene films, demonstrating that  $\text{Mo}_2\text{Ti}_2\text{C}_3\text{T}_x$  MXene performs plating/stripping terribly in the EMImCl/ $\text{AlCl}_3$  electrolyte. Furthermore, along with the  $\text{Ti}_3\text{C}_2\text{T}_x$ 's compact surface Al deposition, obvious Al metal islands were observed at higher capacities when a microscopic view was taken, suggesting better Al nucleation behaviour when compared to  $\text{Mo}_2\text{Ti}_2\text{C}_3\text{T}_x$  MXene. Overall, XPS, ToF-SIMS, XRD and microscopic analyses are hinting that Al electrodeposition in EMImCl/ $\text{AlCl}_3$  is much favourable and uniform on the  $\text{Ti}_3\text{C}_2\text{T}_x$  MXene as compared to the  $\text{Mo}_2\text{Ti}_2\text{C}_3\text{T}_x$  MXene.

## Further analyses and plausible theories

As all Al-deposited MXenes exhibited some amounts of Al metal or Al<sub>2</sub>O<sub>3</sub> in their XPS and TEM analyses, we can infer that Al metal deposition took place on all samples despite the differences observed. It is known that the key difference between the urea/AlCl<sub>3</sub> and EMImCl/AlCl<sub>3</sub> electrolytes is the presence of [AlCl<sub>2</sub>·(urea)<sub>2</sub>]<sup>+</sup> ions in urea/AlCl<sub>3</sub>. Furthermore, according to previous studies on the urea/AlCl<sub>3</sub> electrolyte,<sup>26</sup> it has been shown that the [AlCl<sub>2</sub>·(urea)<sub>2</sub>]<sup>+</sup> ion can only be reduced to Al metal in the presence of Al<sub>2</sub>Cl<sub>7</sub><sup>-</sup> ions, increasing the complexity of Al deposition.

In general, smoother, and less aggressive protrusions were observed in Al deposits that occurred in the urea/AlCl<sub>3</sub> electrolyte, as compared to the EMImCl/AlCl<sub>3</sub> electrolyte, for both Mo<sub>2</sub>Ti<sub>2</sub>C<sub>3</sub>T<sub>x</sub> and Ti<sub>3</sub>C<sub>2</sub>T<sub>x</sub> MXenes across the different plating capacities. We postulate that this is due to the presence of [AlCl<sub>2</sub>·(urea)<sub>2</sub>]<sup>+</sup> ions in the urea/AlCl<sub>3</sub> electrolyte. Based on the initial DFT calculations, it was observed that the Mo<sub>2</sub>Ti<sub>2</sub>C<sub>3</sub>T<sub>x</sub> MXene enables better adsorption of [AlCl<sub>2</sub>·(urea)<sub>2</sub>]<sup>+</sup> than Ti<sub>3</sub>C<sub>2</sub>T<sub>x</sub> MXene regardless of surface terminations. [AlCl<sub>2</sub>·(urea)<sub>2</sub>]<sup>+</sup> ions may form better initial nucleation sites on MXenes as compared to Al<sub>2</sub>Cl<sub>7</sub><sup>-</sup> ions, thus resulting in the subsequent growth of Al metal islands to be more uniform in the urea/AlCl<sub>3</sub> electrolyte. Furthermore, it is also possible that the Al<sub>2</sub>Cl<sub>7</sub><sup>-</sup> ions enable Al plating on both the MXene film and the Al metal, resulting in deposition occurring on the previously plated Al metal, potentially resulting in aggressive protrusions when the EMImCl/AlCl<sub>3</sub> electrolyte is used. Therefore, while EMImCl/AlCl<sub>3</sub> is a popular electrolyte used in Al electrodeposition, depending on the substrate, its chemical composition might be disadvantageous.

In terms of side reactions, experimentally, it can be deduced that side reactions occur in all 4 different experimental cases. However, as evidenced from the CV curves across cycles, these side reactions are largely electrochemical reversible in the urea/AlCl<sub>3</sub> electrolyte, but potentially irreversible in the EMImCl/AlCl<sub>3</sub> electrolyte, as demonstrated through plating and stripping of aluminium on carbon paper, Mo foil, and Ti<sub>3</sub>C<sub>2</sub>T<sub>x</sub> film. Such irreversible side reactions likely contributed to the instances of CE values exceeding 100 % when the EMImCl/AlCl<sub>3</sub> electrolyte was used, causing the obtained CE values to not adequately reflect the capabilities of the EMImCl/AlCl<sub>3</sub> electrolyte.

Side product-wise, based on our DFT calculations previously, it was observed that [AlCl<sub>2</sub>·(urea)<sub>2</sub>]<sup>+</sup> adsorbs well onto the -O<sub>x</sub> and -F<sub>x</sub> terminated MXenes but less so on the -(OH)<sub>x</sub>-terminated MXenes, whereas the opposite holds for Al<sub>2</sub>Cl<sub>7</sub><sup>-</sup> and AlCl<sub>4</sub><sup>-</sup>. One possible

theory is that the side reactions forming  $\text{Al}(\text{OF})_x$  and  $\text{AlF}_x$  are largely enabled by the  $\text{AlCl}_4^-$  and  $\text{Al}_2\text{Cl}_7^-$ , resulting in the progress of a metal-halogen exchange reaction. Hence, when  $[\text{AlCl}_2 \cdot (\text{urea})_2]^+$  ions are adsorbed on the  $-\text{F}_x$  terminations, the  $-\text{F}_x$  terminations are prevented from further reacting with the other Al-containing complex ions, resulting in the lower  $\text{Al}(\text{OF})_x$  and  $\text{AlF}_x$  contents detected by XPS and TOF-SIMS when the urea/ $\text{AlCl}_3$  electrolyte is used. Therefore, the metal-halogen exchange reaction is further enhanced on the  $\text{Ti}_3\text{C}_2\text{T}_x$  MXene as compared to the  $\text{Mo}_2\text{Ti}_2\text{C}_3\text{T}_x$  MXene, possibly due to the less polarisable electron cloud of Ti as compared to Mo, resulting in weaker Ti-surface termination bonds in  $\text{Ti}_3\text{C}_2\text{T}_x$  MXene with reference to the Mo-surface termination bonds in  $\text{Mo}_2\text{Ti}_2\text{C}_3\text{T}_x$  MXene, thus resulting in  $\text{Ti}_3\text{C}_2\text{T}_x$  MXene having higher  $\text{Al}(\text{OF})_x$  and  $\text{AlF}_x$  contents as compared to  $\text{Mo}_2\text{Ti}_2\text{C}_3\text{T}_x$  MXene.

The theoretical result of  $[\text{AlCl}_2 \cdot (\text{urea})_2]$  adsorbing well onto the  $-\text{O}_x$  and  $-\text{F}_x$  terminated MXenes might also potentially present a trend that  $[\text{AlCl}_2 \cdot (\text{urea})_2]^+$  species adsorb too well on several material substrates as compared to aluminium metal, resulting in relatively lower CE values across all MXenes and control samples as a portion of aluminium was incorporated in the  $[\text{AlCl}_2 \cdot (\text{urea})_2]^+$  ions that are adsorbed strongly on the plated electrode. However, further studies will need to be conducted to determine the generalisability of  $[\text{AlCl}_2 \cdot (\text{urea})_2]^+$  species' adsorption behaviour. Hence, given the presence of side reactions and potentially irreversible reactions, it is likely irrational for MXenes to obtain 100% CE in these two Al-based eutectic electrolytes. However, it is possible for the CE and cycle life of these MXene electrodes to further increase with the help of nanostructures. Alternative separators beyond glass fibre separators might also help to improve the CE and cycle life of these electrodes as DFT calculations show that the adsorption energies of  $\text{SiO}_2$  towards the Al-containing species can be significant (**Figure S15**).<sup>52</sup>

Furthermore, a consistent material behaviour that was observed from all four experimental scenarios was the lack of shift of their respective (002) peaks. This shows that there was no change in interlayer spacings of the MXenes, which is consistent with previous reports involving anion insertion.<sup>53</sup> It is also unlikely for free urea molecules to have been inserted into MXenes as that would have resulted in a peak shift of the MXene XRD pattern as per previous reports.<sup>46</sup> Hence, in these four scenarios, it is likely that intercalation did not take place, or that the interlayer spacings of MXenes were sufficiently large to accommodate the electrolyte species such that further changes to the interlayer spacings were not required.

## Conclusions

Research on room temperature non-aqueous RABs is proceeding slower than other alternative metal batteries because of the inability of its existing electrolytes to take part in the conventional cation-centric nucleation mechanism, rendering its internal battery system more complex than other existing alternative metal batteries. In this work, by using two different MXene films (i.e.,  $\text{Mo}_2\text{Ti}_2\text{C}_3\text{T}_x$  and  $\text{Ti}_3\text{C}_2\text{T}_x$ ) with differing amounts of metal-surface termination bond strengths, termination group compositions, and interlayer spacing, we could amplify and gain deeper insights regarding the tangible differences between two popular Al-based eutectic electrolytes (i.e., urea/ $\text{AlCl}_3$  and EMImCl/ $\text{AlCl}_3$ ). While recent works have reported good Al plating and stripping characteristics when the EMImCl/ $\text{AlCl}_3$  electrolyte is used, the prevalence of CE values exceeding 100 % and inconsistent CV curves show that the EMImCl/ $\text{AlCl}_3$  electrolyte is still innately far from being a good versatile Al-based electrolyte that can easily integrate into existing commercial practices, going beyond the usual reasons of corrosion provided in existing literature. Hence, despite the numerous reports of EMImCl/ $\text{AlCl}_3$ 's good metal plating and stripping performance, further in-depth studies should be conducted in future EMImCl/ $\text{AlCl}_3$  works to better understand the underlying electrolyte mechanism, therefore allowing better Al-based electrolytes to be designed.

Beyond the EMImCl/ $\text{AlCl}_3$  electrolyte, this work also demonstrates the potential of the urea/ $\text{AlCl}_3$  electrolyte. Despite its complex dual-ion plating and stripping mechanism and lower average CE than EMImCl/ $\text{AlCl}_3$ , Al plating was observed to be the least aggressive when urea/ $\text{AlCl}_3$  is used on  $\text{Mo}_2\text{Ti}_2\text{C}_3\text{T}_x$  MXene. This plated morphology might be an indication that the urea/ $\text{AlCl}_3$  electrolyte might perform better after undergoing electrode optimisation in later works. The presence of cationic species in urea/ $\text{AlCl}_3$  electrolytes might also be useful in enabling the integration of non-aqueous RABs into existing battery material technologies. Overall, due to the characteristics of Al, research to obtain a good room temperature non-aqueous RAB will likely involve different mechanisms as compared to conventional metal batteries, resulting in the need for audacious attempts toward system understanding and manipulation.

## Experimental procedures

### Synthesis of $\text{Mo}_2\text{Ti}_2\text{C}_3\text{T}_x$ and $\text{Ti}_3\text{C}_2\text{T}_x$ MXene

To synthesise  $\text{Mo}_2\text{Ti}_2\text{C}_3\text{T}_x$  MXene, 1 g of  $\text{Mo}_2\text{Ti}_2\text{AlC}_3$  MAX phase was mixed with 10 mL of hydrofluoric acid (HF, 49-51 wt% concentration, Sigma-Aldrich) solution as an etchant in a high-density polyethylene bottle, and stirred at 300 rpm for 96 h at 55 °C. The etched multilayered  $\text{Mo}_2\text{Ti}_2\text{C}_3\text{T}_x$  MXene flakes were washed with deionised water through repeated centrifugation and decantation in an Eppendorf centrifuge at 3234 RCF (4-5 cycles with ~200 mL of deionised water) until the supernatant reached pH ~ 6.

To delaminate, the etched multilayer  $\text{Mo}_2\text{Ti}_2\text{C}_3\text{T}_x$  MXene sediment was added to 5 mL of tetramethylammonium hydroxide (TMAOH) solution (25 wt% stock, Fisher Scientific) in 15 mL of deionized water per gram of MAX. The mixture of TMAOH and etched multilayered MXene was then stirred at 300 rpm for 4 h at 55 °C. After delamination, the  $\text{Mo}_2\text{Ti}_2\text{C}_3\text{T}_x$  MXene solution was washed to neutral pH via repeated centrifugation and decantation in the Thermo Scientific centrifuge at 21913 RCF (4 cycles with ~200 mL of deionised water). Thereafter, the final mixture was re-dispersed in 15 mL of deionized water and vortexed for 15 minutes. The suspension was then centrifuged in the Thermo Scientific centrifuge at 2795 RCF for 30 minutes to ensure the  $\text{Mo}_2\text{Ti}_2\text{C}_3\text{T}_x$  MXene solutions were single to few-layered flakes. The final suspension of  $\text{Mo}_2\text{Ti}_2\text{C}_3\text{T}_x$  from the supernatant was collected and stored in freezer at -20 °C until use.

To synthesise  $\text{Ti}_3\text{C}_2\text{T}_x$  MXene, 1 g of optimised  $\text{Ti}_3\text{AlC}_2$  MAX was first washed using 9 M HCl for 18 h to remove intermetallic impurities and mixed with an etchant solution (6:3:1 mixture (by volume) of 12 M HCl, DI water, and 50 wt % HF (Acros Organics, Fair Lawn, NJ)) before stirring at 400 rpm for 24 h at 35 °C.<sup>32,54</sup> The etched  $\text{Ti}_3\text{C}_2\text{T}_x$  MXene was washed with deionised water via repeated centrifugation at 3234 RCF (4-5 cycles with ~200 mL of deionised water) until the supernatant reached pH ~ 6. For delamination, the etched multilayered  $\text{Ti}_3\text{C}_2\text{T}_x$  MXene sediment was then added to LiCl (typically 50 mL/per gram of starting etched powder) solution. The mixture of LiCl and multilayer MXene was then stirred at 400 rpm for 1 h at 65 °C under constant argon gas flow. The mixture was then washed with deionised water via centrifugation at 3234 RCF for 5, 10, 15 and 20 minutes. Then, the final mixture was vortexed for 30 minutes followed by centrifugation at 2380 RCF for 30 minutes to ensure the MXene solutions were single-to-few-layered flakes. The final suspension of  $\text{Ti}_3\text{C}_2\text{T}_x$  MXene was collected and stored in the freezer at -20 °C until use.

### Preparation of $\text{Mo}_2\text{Ti}_2\text{C}_3\text{T}_x$ and $\text{Ti}_3\text{C}_2\text{T}_x$ MXene freestanding films

30 mg of previously freeze-dried MXene powders were added to 10 mL of deaerated DI water and sonicated for 1 min to form a MXene suspension. Vacuum filtration of the obtained MXene suspension was conducted on Celgard 3501 membrane (11 Technology Co., Ltd.). The obtained film was frozen in liquid nitrogen and freeze-dried at -50°C, 158 mT to obtain the final freestanding MXene films.

## Material characterization

Micromorphology images were observed on a JEOL 7600F scanning electron microscopy (SEM) equipped with an Oxford Technology X-ray detector and FEI Talos f200x transmission electron microscopy (TEM).  $^{27}\text{Al}$  NMR was conducted on Bruker AVANCE NEO 600M. Zeta potential analyses were conducted using the NanoBrook Omni. The elemental analysis and chemical composition of samples were characterized by X-ray photoelectron spectroscopy (Thermo Fisher Scientific, with Al  $K\alpha$  radiation of 1486.6 eV), X-ray diffraction (Bruker D8 with Cu  $K\alpha$  radiation,  $\lambda = 1.5418 \text{ \AA}$ ) and time-of-flight secondary ion mass spectrometry (IONTOF GmbH, Germany measurements) were conducted as well. The cycled electrodes were disassembled and washed with DMC solvent for further analysis in an Ar-filled glove box ( $\text{H}_2\text{O} < 0.1 \text{ ppm}$ ,  $\text{O}_2 < 0.1 \text{ ppm}$ ). Airtight sample holders were used to transfer samples from the glove box to the sample chamber.

## Electrochemical Measurements

Swagelok cells were assembled with an Ar-filled glove box using Aluminium foils (1.0 mm thick, annealed, 99.99% (metal basis), Thermo Scientific Chemicals), GF/D separators, and MXene electrodes. Glassy carbon disks were placed at the ends of the internal Swagelok to prevent potential corrosion. The urea/ $\text{AlCl}_3$  and EMImCl/ $\text{AlCl}_3$  electrolytes were prepared using 99.0% urea powder (Sigma Aldrich), anhydrous 99.999%  $\text{AlCl}_3$  powder (Sigma Aldrich) and 1-Ethyl-3-methylimidazolium chloride (dry,  $\geq 98.0\%$  (T), Sigma Aldrich). Plating and stripping cyclic voltammetry (CV) curves of the Swagelok cells were recorded on an EC-Lab electrochemical workstation in the range between 0.9 V and -0.4 V vs Al/ $\text{Al}^{3+}$  at room temperature at a scan rate of 1 mV/s. Galvanostatic discharge-charge tests of the Swagelok cells were carried out using the NEWARE Battery Measurement System.

## Density functional theory (DFT) calculations

All DFT+U calculations are calculated using the Perdew, Burke, and Ernzerhof (PBE) exchange-correlation functional implemented in Vienna Ab-initio Simulation Package (version 5.4).<sup>55,56</sup> The projector augmented wave (PAW) method is used for describing the core-valence interaction. The rotationally invariant approach using the U parameters is utilized to correct the effects from the strongly correlated electrons in transition metal ions. The adopted U values for Mo and Ti are 4.0 and 4.2, respectively.<sup>57-61</sup> The kinetic energy cutoff for the plane-wave expansion is set at 600 eV. The Gamma sampling of a  $3 \times 3 \times 1$   $k$ -point grid is used for the slabs. During geometry optimizations, the bottom two layers of atoms in the slabs are frozen and the lattices are kept fixed at the optimized bulk values. The rest of the ions are fully relaxed until the total energy and absolute value of the forces acting on each atom are less than  $1 \times 10^{-6} \text{ eV}$  and  $2 \times 10^{-2} \text{ eV \AA}^{-1}$ , respectively. A vacuum layer of at least 15  $\text{\AA}$  and dipole corrections are applied. The DFT-D3 method is used to correct the dispersion interactions. The Al molecules are optimized within a  $20 \times 20 \times 20 \text{ \AA}^3$  box with the Gamma only sampling. The adsorption energy ( $E_a$ ) is calculated using the equation:  $E_a = E_{surf+mol} - (E_{surf} + E_{mol})$  where  $E_{surf+mol}$ ,

$E_{surf}$  and  $E_{mol}$  are the total energies of the Al molecule adsorbed slab, the pristine slab and the Al molecule, respectively.<sup>62</sup> The more negative the adsorption energy, the stronger the adsorption strength.

### Author Contributions

W.Y. Lieu, A. Thakur, S. Kumar contributed equally to this work and did most of the experiments. Y. Li, X. L. Li, Y. Li, Y. Li, and G. Yang contributed to the characterisation of battery performance and the interpretation of results. T. Ghosh conducted TEM analysis and M. Ng conducted the DFT simulations. B. Anasori, H. Y. Yang, and Z. W. Seh supervised this project, and this manuscript was reviewed by all authors prior to submission.

### Acknowledgements

This work is supported by the Singapore National Research Foundation (NRF Investigatorship NRF-NRFI09-0002), the Agency for Science, Technology and Research (MTC Programmatic Fund M23L9b0052 and Central Research Fund Award), and the Singapore Ministry of Education academic research grant Tier 2 (MOE2019-T2-1-181). We acknowledge the National Supercomputing Centre (NSCC) Singapore and A\*STAR Computational Resource Centre (A\*CRC) of Singapore with its high-performance computing facilities. We also thank Zhenxiang Xing and Debbie Hwee Leng Seng for assistance with TOF-SIMS and XPS measurements respectively.

### References

1. Li, M., Lu, J., Ji, X.L., Li, Y.G., Shao, Y.Y., Chen, Z.W., Zhong, C., and Amine, K. (2020). Design strategies for nonaqueous multivalent-ion and monovalent-ion battery anodes. *Nat. Rev. Mater.* **5**, 276-294. 10.1038/s41578-019-0166-4.
2. Liang, Y.L., Dong, H., Aurbach, D., and Yao, Y. (2020). Current status and future directions of multivalent metal-ion batteries. *Nat. Energy* **5**, 822-822. 10.1038/s41560-020-0676-8.
3. Ng, K.L., Amrithraj, B., and Azimi, G. (2022). Nonaqueous rechargeable aluminum batteries. *Joule* **6**, 134-170. 10.1016/j.joule.2021.12.003.
4. Tu, J., Song, W.L., Lei, H.P., Yu, Z.J., Chen, L.L., Wang, M.Y., and Jiao, S.Q. (2021). Nonaqueous Rechargeable Aluminum Batteries: Progresses, Challenges, and Perspectives. *Chem. Rev.* **121**, 4903-4961. 10.1021/acs.chemrev.0c01257.
5. Xu, K. (2014). Electrolytes and Interphases in Li-Ion Batteries and Beyond. *Chem. Rev.* **114**, 11503-11618. 10.1021/cr500003w.
6. Han, M.M., Li, T.C., Li, D.S., and Yang, H.Y. (2023). Electrolyte Modulation Strategies for High Performance Zinc Batteries. *Batteries Supercaps* **6**, e202200560. 10.1002/batt.202200560.
7. Meng, Y.S., Srinivasan, V., and Xu, K. (2022). Designing better electrolytes. *Science* **378**, eabq3750. 10.1126/science.abq3750.
8. Chao, D.L., Zhou, W.H., Xie, F.X., Ye, C., Li, H., Jaroniec, M., and Qiao, S.Z. (2020). Roadmap for advanced aqueous batteries: From design of materials to applications. *Sci. Adv.* **6**, eaba4098. 10.1126/sciadv.aba4098.
9. Cohn, G., Ma, L., and Archer, L.A. (2015). A novel non-aqueous aluminum sulfur battery. *J. Power Sources* **283**, 416-422. 10.1016/j.jpowsour.2015.02.131.
10. Elia, G.A., Marquardt, K., Hoeppe, K., Fantini, S., Lin, R.Y., Knipping, E., Peters, W., Drillet, J.F., Passerini, S., and Hahn, R. (2016). An Overview and Future Perspectives of Aluminum Batteries. *Adv. Mater.* **28**, 7564-7579. 10.1002/adma.201601357.

11. Han, M.M., Zhou, J., and Fan, H.J. (2023). Opportunity for eutectic mixtures in metal-ion batteries. *Trends Chem.* **5**, 214-224. 10.1016/j.trechm.2023.01.003.
12. Jayaprakash, N., Das, S.K., and Archer, L.A. (2011). The rechargeable aluminum-ion battery. *Chem. Comm.* **47**, 12610-12612. 10.1039/c1cc15779e.
13. Lin, M.C., Gong, M., Lu, B.G., Wu, Y.P., Wang, D.Y., Guan, M.Y., Angell, M., Chen, C.X., Yang, J., Hwang, B.J., and Dai, H.J. (2015). An ultrafast rechargeable aluminium-ion battery. *Nature* **520**, 325-328. 10.1038/nature14340.
14. Pan, C.J., Yuan, C.Z., Zhu, G.Z., Zhang, Q., Huang, C.J., Lin, M.C., Angell, M., Hwang, B.J., Kaghazchi, P., and Dai, H.J. (2018). An operando X-ray diffraction study of chloroaluminate anion-graphite intercalation in aluminum batteries. *Proc. Natl. Acad. Sci. U.S.A.* **115**, 5670-5675. 10.1073/pnas.1803576115.
15. Wang, D.Y., Wei, C.Y., Lin, M.C., Pan, C.J., Chou, H.L., Chen, H.A., Gong, M., Wu, Y.P., Yuan, C.Z., Angell, M., et al. (2017). Advanced rechargeable aluminium ion battery with a high-quality natural graphite cathode. *Nat. Commun.* **8**, 14283-14290. 10.1038/ncomms14283.
16. Zhao, X., Zhao-Karger, Z., Fichtner, M., and Shen, X. (2020). Halide-Based Materials and Chemistry for Rechargeable Batteries. *Angewandte Chemie International Edition* **59**, 5902-5949. 10.1002/anie.201902842.
17. Xue, Z., Gao, Z., and Zhao, X. (2022). Halogen Storage Electrode Materials for Rechargeable Batteries. *ENERGY & ENVIRONMENTAL MATERIALS* **5**, 1155-1179. 10.1002/eem2.12442.
18. Geng, L.S., Wang, X.P., Han, K., Hu, P., Zhou, L., Zhao, Y.L., Luo, W., and Mai, L.Q. (2022). Eutectic Electrolytes in Advanced Metal-Ion Batteries. *ACS Energy Lett.* **7**, 247-260. 10.1021/acseenergylett.1c02088.
19. Faegh, E., Ng, B., Hayman, D., and Mustain, W.E. (2021). Practical assessment of the performance of aluminium battery technologies. *Nat. Energy* **6**, 450-450. 10.1038/s41560-021-00791-z.
20. Kumar, S., Rama, P., Yang, G.L., Lieu, W.Y., Chinnadurai, D., and Seh, Z.W. (2023). Additive-Driven Interfacial Engineering of Aluminum Metal Anode for Ultralong Cycling Life. *Nano-Micro Lett.* **15**. 10.1007/s40820-022-01000-6.
21. Kumar, S., Rama, P., Lieu, W.Y., Zhang, C., Busayaporn, W., Chinnadurai, D., Yang, G., Xing, Z., Li, Y., Abbas, Z., et al. (2024). A Bi-based artificial interphase to achieve ultra-long cycling life of Al-metal anode in non-aqueous electrolyte. *Energy Stor. Mater.* **65**, 103087. 10.1016/j.ensm.2023.103087.
22. Angell, M., Pan, C.J., Rong, Y.M., Yuan, C.Z., Lin, M.C., Hwang, B.J., and Dai, H.J. (2017). High Coulombic efficiency aluminum-ion battery using an AlCl<sub>3</sub>-urea ionic liquid analog electrolyte. *Proc. Natl. Acad. Sci. U.S.A.* **114**, 834-839. 10.1073/pnas.1619795114.
23. Angell, M., Zhu, G.Z., Lin, M.C., Rong, Y.M., and Dai, H.J. (2020). Ionic Liquid Analogs of AlCl<sub>3</sub> with Urea Derivatives as Electrolytes for Aluminum Batteries. *Adv. Func. Mater.* **30**, 1901928-1901939. 10.1002/adfm.201901928.
24. Chu, W.Q., Zhang, X., Wang, J., Zhao, S., Liu, S.Q., and Yu, H. (2019). A low-cost deep eutectic solvent electrolyte for rechargeable aluminum-sulfur battery. *Energy Stor. Mater.* **22**, 418-423. 10.1016/j.ensm.2019.01.025.
25. Yang, H.C., Yin, L.C., Liang, J., Sun, Z.H., Wang, Y.Z., Li, H.C., He, K., Ma, L.P., Peng, Z.Q., Qiu, S.Y., et al. (2018). An Aluminum-Sulfur Battery with a Fast Kinetic Response. *Angew. Chem., Int. Ed.* **57**, 1898-1902. 10.1002/anie.201711328.
26. Bian, Y.H., Li, Y., Yu, Z.C., Chen, H., Du, K.W., Qiu, C.C., Zhang, G.X., Lv, Z.C., and Lin, M.C. (2018). Using an AlCl<sub>3</sub>/Urea Ionic Liquid Analog Electrolyte for Improving the Lifetime of Aluminum-Sulfur Batteries. *Chemelectrochem* **5**, 3607-3611. 10.1002/celec.201801198.
27. Ng, K.L., Malik, M., Buch, E., Glossmann, T., Hintennach, A., and Azimi, G. (2019). A low-cost rechargeable aluminum/natural graphite battery utilizing urea-based ionic liquid analog. *Electrochim. Acta* **327**, 135031-135042. 10.1016/j.electacta.2019.135031.
28. Elia, G.A., Hoeppepner, K., and Hahn, R. (2021). Comparison of Chloroaluminate Melts for Aluminum Graphite Dual-Ion Battery Application. *Batteries Supercaps* **4**, 368-373. 10.1002/batt.202000244.

29. Smith, E.L., Abbott, A.P., and Ryder, K.S. (2014). Deep Eutectic Solvents (DESS) and Their Applications. *Chem. Rev.* **114**, 11060-11082. 10.1021/cr300162p.
30. Watanabe, M., Thomas, M.L., Zhang, S.G., Ueno, K., Yasuda, T., and Dokko, K. (2017). Application of Ionic Liquids to Energy Storage and Conversion Materials and Devices. *Chem. Rev.* **117**, 7190-7239. 10.1021/acs.chemrev.6b00504.
31. Lipatov, A., Lu, H.D., Alhabeab, M., Anasori, B., Gruverman, A., Gogotsi, Y., and Sinitskii, A. (2018). Elastic properties of 2D Ti<sub>3</sub>C<sub>2</sub>T<sub>x</sub> MXene monolayers and bilayers. *Sci. Adv.* **4**, eaat0491. 10.1126/sciadv.aat0491.
32. Thakur, A., Chandran B.S., N., Davidson, K., Bedford, A., Fang, H., Im, Y., Kanduri, V., Wyatt, B.C., Nemani, S.K., Poliukhova, V., et al. (2023). Step-by-Step Guide for Synthesis and Delamination of Ti<sub>3</sub>C<sub>2</sub>T<sub>x</sub> MXene. *Small Methods* **7**, 2300030. 10.1002/smt.202300030.
33. Shayesteh Zeraati, A., Mirkhani, S.A., Sun, P., Naguib, M., Braun, P.V., and Sundararaj, U. (2021). Improved synthesis of Ti<sub>3</sub>C<sub>2</sub>T<sub>x</sub> MXenes resulting in exceptional electrical conductivity, high synthesis yield, and enhanced capacitance. *Nanoscale* **13**, 3572-3580. 10.1039/D0NR06671K.
34. Lim, K.R.G., Shekhiriev, M., Wyatt, B.C., Anasori, B., Gogotsi, Y., and Seh, Z.W. (2022). Fundamentals of MXene synthesis. *Nat. Synth.* **1**, 601-614. 10.1038/s44160-022-00104-6.
35. Anasori, B., Lukatskaya, M.R., and Gogotsi, Y. (2017). 2D metal carbides and nitrides (MXenes) for energy storage. *Nat. Rev. Mater.* **2**, 16098. 10.1038/natrevmats.2016.98.
36. Gogotsi, Y., and Anasori, B. (2019). The Rise of MXenes. *ACS Nano* **13**, 8491-8494. 10.1021/acsnano.9b06394.
37. Li, Y.J., Feng, X., Lieu, W.Y., Fu, L., Zhang, C., Ghosh, T., Thakur, A., Wyatt, B.C., Anasori, B., Liu, W., et al. (2023). MXene-Based Anode-Free Magnesium Metal Battery. *Adv. Func. Mater.* 10.1002/adfm.202303067.
38. Li, Y.J., Lieu, W.Y., Ghosh, T., Fu, L., Feng, X., Wong, A.J.Y., Thakur, A., Wyatt, B.C., Anasori, B., Zhang, Q.F., et al. (2023). Double-Transition-Metal MXene Films Promoting Deeply Rechargeable Magnesium Metal Batteries. *Small Methods* **7**, 2201598-2201606. 10.1002/smt.202201598.
39. Lim, K.R.G., Handoko, A.D., Nemani, S.K., Wyatt, B., Jiang, H.Y., Tang, J.W., Anasori, B., and Seh, Z.W. (2020). Rational Design of Two-Dimensional Transition Metal Carbide/Nitride (MXene) Hybrids and Nanocomposites for Catalytic Energy Storage and Conversion. *ACS Nano* **14**, 10834-10864. 10.1021/acsnano.0c05482.
40. Guan, W., Huang, Z., Wang, W., Song, W.L., Tu, J.G., Luo, Y.W., Lei, H.P., Wang, M.Y., and Jiao, S.Q. (2023). The Negative-Charge-Triggered "Dead Zone" between Electrode and Current Collector Realizes Ultralong Cycle Life of Aluminum-Ion Batteries. *Adv. Mater.*, 2205489-2205502. 10.1002/adma.202205489.
41. Yuan, Z.Y., Lin, Q.F., Li, Y.L., Han, W., and Wang, L.L. (2023). Effects of Multiple Ion Reactions Based on a CoSe<sub>2</sub>/MXene Cathode in Aluminum-Ion Batteries. *Adv. Mater.* **35**, 2211527-2211535. 10.1002/adma.202211527.
42. Liu, X.J., Tu, S.B., Li, J.H., Zeng, F.S., El-Demellawi, J.K., Lin, Q.C., Xi, S.K., Wu, J.W., Tang, J.C., and Zhang, X.X. (2022). Nb<sub>2</sub>CT<sub>x</sub> MXene Cathode for High-Capacity Rechargeable Aluminum Batteries with Prolonged Cycle Lifetime. *ACS Appl. Mater. Inter.*, 45254-45262. 10.1021/acсами.2c09765.
43. VahidMohammadi, A., Hadjikhani, A., Shahbazmohamadi, S., and Beidaghi, M. (2017). Two-Dimensional Vanadium Carbide (MXene) as a High-Capacity Cathode Material for Rechargeable Aluminum Batteries. *ACS Nano* **11**, 11135-11144. 10.1021/acsnano.7b05350.
44. Huo, X.G., Wang, X.X., Li, Z.Y., Liu, J., and Li, J.L. (2020). Two-dimensional composite of D-Ti<sub>3</sub>C<sub>2</sub>T<sub>x</sub>@S@TiO<sub>2</sub> (MXene) as the cathode material for aluminum-ion batteries. *Nanoscale* **12**, 3387-3399. 10.1039/c9nr09944a.
45. Malik, M., Ng, K.L., and Azimi, G. (2020). Physicochemical characterization of AlCl<sub>3</sub>-urea ionic liquid analogs: Speciation, conductivity, and electrochemical stability. *Electrochim. Acta* **354**, 136708-136720. 10.1016/j.electacta.2020.136708.
46. Overbury, S.H., Kolesnikov, A.I., Brown, G.M., Zhang, Z., Nair, G.S., Sacci, R.L., Lotfi, R., van Duin, A.C.T., and Naguib, M. (2018). Complexity of Intercalation in MXenes:

- Destabilization of Urea by Two-Dimensional Titanium Carbide. *J. Am. Chem. Soc.* **140**, 10305-10314. 10.1021/jacs.8b05913.
47. Halim, J., Cook, K.M., Naguib, M., Eklund, P., Gogotsi, Y., Rosen, J., and Barsoum, M.W. (2016). X-ray photoelectron spectroscopy of select multi-layered transition metal carbides (MXenes). *Appl. Surf. Sci.* **362**, 406-417. 10.1016/j.apsusc.2015.11.089.
  48. Wu, M.S., Xu, B., Chen, L.Q., and Ouyang, C.Y. (2016). Geometry and fast diffusion of  $\text{AlCl}_4$  cluster intercalated in graphite. *Electrochim. Acta* **195**, 158-165. 10.1016/j.electacta.2016.02.144.
  49. Meng, Y.H., Wang, M.M., Li, K., Zhu, Z.X., Liu, Z.C., Jiang, T.L., Zheng, X.H., Zhang, K., Wang, W.P., Peng, Q., et al. (2023). Reversible, Dendrite-Free, High-Capacity Aluminum Metal Anode Enabled by Aluminophilic Interface Layer. *Nano Lett.* **23**, 2295-2303. 10.1021/acs.nanolett.2c05077.
  50. Zhao, Q., Zheng, J.X., Deng, Y., and Archer, L. (2020). Regulating the growth of aluminum electrodeposits: towards anode-free Al batteries. *J. Mater. Chem. A* **8**, 23231-23238. 10.1039/d0ta08505g.
  51. Elia, G.A., Hasa, I., Greco, G., Diemant, T., Marquardt, K., Hoepfner, K., Behm, R.J., Hoell, A., Passerini, S., and Hahn, R. (2017). Insights into the reversibility of aluminum graphite batteries. *J. Mater. Chem. A* **5**, 9682-9690. 10.1039/c7ta01018d.
  52. Elia, G.A., Ducros, J.-B., Sotta, D., Delhorbe, V., Brun, A., Marquardt, K., and Hahn, R. (2017). Polyacrylonitrile Separator for High-Performance Aluminum Batteries with Improved Interface Stability. *ACS Appl. Mater. Inter.* **9**, 38381-38389. 10.1021/acsami.7b09378.
  53. Shpigel, N., Chakraborty, A., Malchik, F., Bergman, G., Nimkar, A., Gavriel, B., Turgeman, M., Hong, C.N., Lukatskaya, M.R., Levi, M.D., et al. (2021). Can Anions Be Inserted into MXene? *J. Am. Chem. Soc.* **143**, 12552-12559. 10.1021/jacs.1c03840.
  54. Mathis, T.S., Maleski, K., Goad, A., Sarycheva, A., Anayee, M., Foucher, A.C., Hantanasirisakul, K., Shuck, C.E., Stach, E.A., and Gogotsi, Y. (2021). Modified MAX Phase Synthesis for Environmentally Stable and Highly Conductive  $\text{Ti}_3\text{C}_2$  MXene. *ACS Nano* **15**, 6420-6429. 10.1021/acsnano.0c08357.
  55. Perdew, J.P., Burke, K., and Ernzerhof, M. (1996). Generalized gradient approximation made simple. *Phys Rev Lett* **77**, 3865-3868. DOI 10.1103/PhysRevLett.77.3865.
  56. Kresse, G., and Furthmüller, J. (1996). Efficient iterative schemes for ab initio total-energy calculations using a plane-wave basis set. *Phys Rev B* **54**, 11169-11186. DOI 10.1103/PhysRevB.54.11169.
  57. Blochl, P.E. (1994). Projector Augmented-Wave Method. *Phys Rev B* **50**, 17953-17979. DOI 10.1103/PhysRevB.50.17953.
  58. Anisimov, V.I., Zaanen, J., and Andersen, O.K. (1991). Band Theory and Mott Insulators - Hubbard-U Instead of Stoner-I. *Phys Rev B* **44**, 943-954. DOI 10.1103/PhysRevB.44.943.
  59. Dudarev, S.L., Botton, G.A., Savrasov, S.Y., Humphreys, C.J., and Sutton, A.P. (1998). Electron-energy-loss spectra and the structural stability of nickel oxide: An LSDA+U study. *Phys Rev B* **57**, 1505-1509. DOI 10.1103/PhysRevB.57.1505.
  60. Shao, P.H., Chang, Z.W., Li, M., Lu, X., Jiang, W.L., Zhang, K., Luo, X.B., and Yang, L.M. (2023). Mixed-valence molybdenum oxide as a recyclable sorbent for silver removal and recovery from wastewater. *Nat. Commun.* **14**. 10.1038/s41467-023-37143-2.
  61. Wang, D.S., Li, F., Lian, R.Q., Xu, J., Kan, D.X., Liu, Y.H., Chen, G., Gogotsi, Y., and Wei, Y.J. (2019). A General Atomic Surface Modification Strategy for Improving Anchoring and Electrocatalysis Behavior of  $\text{Ti}_3\text{C}_2\text{T}_x$  MXene in Lithium-Sulfur Batteries. *ACS Nano* **13**, 11078-11086. 10.1021/acsnano.9b03412.
  62. Grimme, S., Antony, J., Ehrlich, S., and Krieg, H. (2010). A consistent and accurate ab initio parametrization of density functional dispersion correction (DFT-D) for the 94 elements H-Pu. *J Chem Phys* **132**. 10.1063/1.3382344.

**TOC:**

# Desired deposition morphology

